Elastic Wave Manipulations via 3D-printed Chains of Hollow Elliptical Cylinders

Hyunryung Kim

A dissertation
submitted in partial fulfillment of the
requirements for the degree of

Doctor of Philosophy

University of Washington

2018

Reading Committee:

Jinkyu Yang, Chair

Richard Wiebe

Marco Salviato

Program Authorized to Offer Degree:
Aeronautics and Astronautics

University of Washington

Abstract

Elastic Wave Manipulations via 3D-printed Chains of Hollow Elliptical Cylinders

Hyunryung Kim

Chair of the Supervisory Committee:
Professor Jinkyu Yang
Department of Aeronautics and Astronautics

Lattice structures have been studied for a long time but have come into spotlight in recent years as a test bed for various wave manipulations. Researchers have started to pay attention not only to their interesting static/dynamic behaviors but also to their high tunability. In this work, we explore linear and nonlinear elastic wave dynamics in lattice chains. Specifically, the chains are composed of 3D-printed hollow elliptical cylinders (HECs). 3D-printing provides us the freedom of altering the design of the HECs, hence offering high tunability of the HEC lattice chains. This implies that we can assemble different systems for various wave manipulations. First, we investigate shock wave propagation in the homogeneous chain. We experimentally and numerically demonstrate the formation of dispersive rarefaction shocks in the 3D-printed soft HEC chain. We claim that the dispersion in the wave tails and the rarefaction in the leading pulse of the dispersive rarefaction shocks provide innate advantage in energy absorption. Next, we consider graded chains made of HECs with varying thicknesses, where asymmetric wave dynamics is invoked. In the decreasing thickness chain, we find out that elastic waves are trapped at a specific location of the chain, which is based on the principle of the Bloch oscillations. This trapping mechanism depends on the input frequency of the propagating elastic waves. In the increasing thickness chain, however, we observe waves are reflected back in the middle of the chain whose location depends on the input frequency. Finally, we show asymmetric nonlinear wave dynamics in the graded HEC

chain. Under the same striker impact, the wave decelerates in the decreasing thickness chain whereas it accelerates in the increasing thickness chain. We discover that there is near an order-of-magnitude difference in transmitted force between these two directions. We extend our findings from the 1D systems to a 2D lattice, with a possibility of using it as a core material in sandwich structures. These results suggest that the 3D-printed HECs can be built into different structures to manipulate mechanical waves in various ways, such as attenuation, localization, and filtering. We can exploit the findings in this work for potential applications in impact mitigation, vibration isolation, and energy harvesting.

TABLE OF CONTENTS

LIST OF FIGURES

LIST OF TABLES

ACKNOWLEDGMENTS

First of all, I would like to express my appreciation to my doctoral advisor, Professor Jinkyu Yang, for providing valuable guidance and sharing insights in this research project. I also would like to thank my Ph.D. committee, Prof. Marco Salviato, Prof. Tony Waas, Prof. Richard Wiebe, Prof. Behcet Acikmese, Prof. Nicholas Boechler, Prof. Antonino Ferrante, and Prof. Mehran Mesbahi for providing constructive comments and suggestions.

Also, I would like to thank my research collaborators. Prof. Panayotis G. Kevrekidis (University of Massachusetts), Prof. Christopher Chong (Bowdoin College), and Dr. Efstathios G. Charalampidis (University of Massachusetts) enlightened me with their mathematical knowledge. I would like to give special thanks to Prof. Eunho Kim (Chonbuk National University, Korea) for guiding my research from afar since the beginning of the HEC project.

Furthermore, I would like to show my gratitude for technical support. Prof. Carl Knowlen (University of Washington) and Prof. Tony Waas (University of Michigan) generously let me use their high speed camera equipment for my research. Dennis Wise (University Marketing & Communications) lent me his studio light, which was an immense help for conducting my experiment successfully. Dzung Tran (University of Washington A&A Machine Shop) kindly helped machine metals for experiments. Francesca Green (University of Washington) gave me a big helping hand in learning 3D-printing as an undergraduate intern. Waverly Harden (Bowdoin College) was a very passionate mathematics student who helped numerical modeling over a summer. Pai Wang (Harvard University) generously shared his Python and Fortran scripts for ABAQUS, which extremely accelerated my research progress.

I met a wonderful group of people, the members of the Laboratory for Engineered Mate-

rials and Structures (LEMS). Dr. Hiromi Yasuda and Dr. Rajesh Chaunsali were not only outstanding researchers, but also great friends from the beginning to the end of this journey. They kept me motivated in various aspects of my Ph.D. student life. Also, I would like to say special thanks to Xiaotian Shi (Oliver) for being a wonderful collaborator in several projects. I also thank the LEMS members and visitors, Chun-Wei Chen, Seunghyun Ko, James O'Neil, Qingqian Li, Koshiro Yamaguchi, Yasuhiro Miyazawa, Rohith Jayaram, Kosei Tsujikawa, Balakumaran Gopalarethinam, Dr. Yang Nan, Prof. Gil-Yong Lee, Prof. Rui Zhu, Aman Thakkar, Noel Kimber, Joshua Rivey, Taru Singhal, Matthew Toles, Mohamed Ghanem, Sean Phenisee, Dr. Hyung-Joon Bang, Ying Wu, Cheng Luo, Mia Lee, Zhisong Chen and all others, for keeping me company at the lab.

This long journey would not have been completed without support from my dearest friends. Yurim Lee has been my best friend since the day I arrived at Seattle. We shared many thoughts of life matters, ups and downs of a Ph.D. student, and drinks. She was the one I shared my concerns with, knowing that she would understand me entirely. I also met wonderful new friends, Shuya Yuan, Zhaozhao Liu, and Elise Tran, in my first year and our friendship has been so strong ever since. We made great memories together and always supported each other. Needless to say, my good old friends from college, Yunha Ryu, Suji Kim, and Dasom Yang, cheered me on from afar and have been life consultants for each other. Last but not least, my biggest supporter, David Chi, was so thoughtful, understanding, caring, and loving. I sincerely appreciate him with all my heart.

Lastly, I send huge thanks to my family. My mom and dad gave me unconditional love and belief in me. My only and proud brother and his wife, were there for me whenever I needed them. My lovely one-year-old twin nephews were the source of my biggest smiles. My grandfather and grandmother have been keeping themselves healthy to wish me a good luck. My aunts, uncles, and cousins have all been big fans of me, cheering me on.

DEDICATION

to my family and David Chi.

Chapter 1

INTRODUCTION

Wave manipulation is a very common part in our daily lives. For instance, people use protective enclosures for their small electronics such as cell phones, tablet PCs, or laptops. Alternatively, vehicles or aircraft that surround us everyday have been designed to protect us from injury. All of these are examples of *impact mitigation*. Impact mitigation is a mechanism that attenuates the input energy significantly to secure any object of interest. But this is not the only type of wave manipulation. Another type is *filtering*, which lets only desired frequencies pass through the system. This can include noise reducers or pop filters. *Localization* is yet another type of wave manipulation, in which we lock the energy at a designated spot within a system. An example of this is solar panel design where we want to increase the efficiency by collecting the energy in a small area.

Researchers have attempted to demonstrate these kinds of wave manipulation in mechanical systems. In demonstrating *impact mitigation*, Uehara *et al.* found that a bed full of granular media effectively attenuates the impact by dissipating energy through inelastic collisions or frictions between granules [4]. Meanwhile for *filtering*, Martinez-Sala *et al.* discovered acoustic filtering capability from a sculpture art [5, 6]. Demonstrating *localization*, Carrara *et al.* devised energy harvesting system, an elliptical acoustic mirror, to focus incoming waves into the focal point of the ellipse [7].

Furthermore, in the following three sections, we dive deep into examples of elastic wave manipulations - shock wave creation, impact mitigation, and wave localization in mechanical systems.

The texts in this chapter have been partly taken from the author's publication [1] and archived manuscripts on arXiv [2, 3].

1.1 Dispersive rarefaction shock waves

Computational and experimental investigation of mechanical waves propagating in nonlinear lattices has been a subject of intense research in recent decades. Primary efforts have been placed on exploring solitary traveling waves [8, 9] and discrete breathers [10, 11]; see also [12, 13]. Arguably, less attention has been paid to the possibility of shock wave formation, especially at the experimental level within the realm of granular crystals and mechanical metamaterials [14–17]. Herbold and Nesterenko investigated the formation of shock waves under the influence of viscous dissipation [14]. Molinari *et al.* [15] studied dispersive shock waves in uniform and periodic heterogeneous granular crystals, which feature oscillatory wave tails following the steady shock front. Shocks in disordered granular crystals were also studied in [16]. In these studies, granular lattice elements interact with each other under the effective strain-hardening power law (i.e., compressive force F and displacement δ have $F \sim \delta^p$ where the nonlinear exponent $p > 1$) [18].

If a discrete system can exhibit effective strain-softening behaviors ($p < 1$), we can anticipate the emergence of distinctive features in comparison to the case of $p > 1$. For instance, Herbold *et al.* reported theoretical observation of rarefaction waves, which form tensile wavefronts despite the application of compressive impact [19]. More recently, Yasuda *et al.* demonstrated numerically the formation of waves that combine a dispersive shock tail and a rarefaction front wave, so-called *dispersive rarefaction shocks* (DRS), by using generalized power-law contact models [20]. These studies, however, have been conducted without experimental verification, though the experimental feasibility has been discussed in tensegrity [21] and origami [22] platforms. If we can realize a physical system that supports the DRS, it would enable a two-fold efficient impact mitigation system for attenuating stress waves: one by transitioning the steep shock wavefront into a back-tilted form (within the *rarefaction* due to the extension of the wavefront width) and the other by distributing energy to oscillatory tails over the space domain (within the *dispersive shock*).

1.2 Bloch oscillations in graded chains

Bloch oscillation describes interesting quantum mechanics of electrons. When an external electric field is applied at a constant power, electrons in a periodic potential show spatially localized oscillations [23, 24]. Kohn have found that the bands stemming from the periodic field can be changed such that an electrons moves within a band under the applied field [25]. The Bloch oscillation is caused by the equidistant energy band known as the Wannier-Stark ladders [26]. In essence, it is the frequency-domain counterpart of the Bloch oscillation. Despite the prediction of the Bloch oscillation in the early twentieth century, it was not until the end of the century that researchers finally observed it. Thanks to the advent of semiconductor superlattices [27], the Wannier-Stark ladders [28,29] and the Bloch oscillations [30–36] were experimentally demonstrated.

Later on, researchers in other field of physics started to show significant interest in the Bloch oscillation. Optical Bloch oscillations have been reported over the last couple of decades [37–43]. The acoustic counterpart has also been explored [44–50]. However, there is a very limited number of published works on the Bloch oscillations of mechanical waves. Gutierrez *et al* [51] studied the Bloch oscillations of torsional waves traveling along the arrays of elastic rods with geometric gradient in their height or width, which mimicked the effect of the electric field on electrons. Arreola-Lucas *et al* [52] also observed the Bloch oscillations of torsional waves passing through a metallic beam with notches which has a gradient in the cavity thickness. In both cases, researchers manufactured their systems by machining metal, which is not favorable for exploring their systems thoroughly by changing design variables. Recently, Shi *et al* [53] came up with a tunable system which realizes the Bloch oscillations of stress waves. They used a chain of solid cylinders with the gradient in their contact angles. This eventually results in the gradient of contact stiffness which creates the Wannier-Stark ladders. It would be beneficial for further study of the Bloch oscillations of elastic waves if we had tunability both in the geometry of components and in the contact stiffness. However, a mechanical system with these aspects is rarely found.

1.3 Impact mitigation in graded chains

Tapered or graded granular chains have been of great interest to researchers for their exceptional impact absorbing ability [9, 54]. First proposed by [55], long tapered granular chains (total number of granular particles, or chain length, $N = 100$) have been shown to reduce their leading pulse's kinetic energy up to 90% compared to monodispersed chains in numerical analysis. Later on, analytic models have been developed [56–59] to describe the physics of the remarkable energy attenuation. Numerical [60] and experimental demonstration [61, 62] have also been reported to claim the feasibility in shorter chains ($N \approx 20$).

Doney *et al.* [63] introduced a superb shock absorbing system, so-called decorated tapered chain (DTC), which mitigates the impact energy significantly in a very short chain length. Supporting experimental results [64] and analytic interpretations [65] have been reported. The challenge with the DTC is that DTC itself is not feasible to be assembled in higher dimensions due to their geometrical constraints. Machado *et al.* [66] found an alternative to DTC by surrounding the regular tapered chain with smaller DTCs. Impulse wave propagation is more attenuated in this quasi-one-dimensional (1D) tapered chain than the regular tapered chain. Ideas of stacking tapered granular chains into two-dimensional (2D) [67] and three-dimensional (3D) [68] space have been proposed recently. However, these studies on tapered granular structures in higher dimensions are limited to numerical investigation, and their experimental demonstration is yet elusive, mainly due to the challenges in their assembly.

One question may arise at this point: can we create a universal system which is capable of all these types of wave manipulation? The key to accomplish this system is to achieve tunability of the system. And recent popularity and intensive development of additive manufacturing, or so-called 3D-printing, could provide a powerful solution to this challenge. 3D-printing technologies have been recently gaining their popularity in various fields as a versatile fabrication tool to create complicated shapes. It gives users a variety of options

in terms of the material, precision, or scale. We can find many fields of study or industry incorporating 3D printing techniques and the elastic wave community is not an exception. There have been a number of studies to design and 3D-print shock-absorbing structures. Tsouknidas *et al.* [69] have evaluated impact absorption of 3D-printed porous polylactic acid (PLA) structures. Bates *et al.* [70] have investigated energy absorption of 3D-printed honeycomb structures made of thermoplastic polyurethane (TPU). Recently, Chen *et al.* [71] have analyzed crushing behavior of graded lattice cylinders, 3D-printed using Acrylonitrile Butadiene Styrene (ABS) plastic, subject to axial impact. Moreover, jumping robots using soft materials [72], compliant structures for carrying vector soliton [73] and for energy trapping [74], and acoustic filter [75] have been reported.

Given these previous explorations, it is more evident that the solution to create a versatile assembly for various wave manipulations can be 3D-printing. Instead of designing different systems for different applications, we would like to design a universal building block to create structures for various wave manipulations. This is analogous to how simple Lego blocks can be built to create different shapes. The design for the building block we propose is hollow elliptical cylinders (HECs). We make them *hollow* to accomplish a light-weight structure. We can also explore the effects of the thickness by leaving them hollow. We choose *ellipse* because it is a general shape of circular objects. By aligning HECs along the major axis, we can achieve all of an ellipse in major axis, a circle, and an ellipse in minor axis under compression. Using this ellipse as a building block will give us various wave dynamics. Curved surfaces of the *cylinders* create a line contact. For this reason, it is easier to assemble a chain or an array with cylinders than it is with spheres which will create a point contact. We can easily change the wave dynamics by tuning the geometry of the HEC cells, which makes the HEC a more universal building block. The tuning geometry part is readily done by 3D-printing, changing the thickness or the shape of the ellipse.

1.4 Organization of the thesis

In Chapter 2, we investigate static behavior of the HECs and linear dynamics of one-dimensional (1D) HEC chain. We apply compressive loads to the HECs and find the force-displacement relationship. We demonstrate the force-displacement relationship by 3D-printing HECs and conducting quasi-static compression tests. We assume a Hertzian contact model to fit the relationship. Additionally, we calculate the dispersion relation of HECs by applying periodic boundary conditions to a unit HEC along the excitation direction. We assume the HEC as a one degree-of-freedom (DOF) spring-mass system and find the cutoff frequency. We verify the effective stiffness obtained from the cutoff frequency is in a similar range of the initial stiffness obtained from the force-displacement relationship.

In Chapter 3, we combine the aforementioned functionalities (shock waves, strain-softening, soft materials) by deploying a soft-lattice system as a prototypical testbed for an experimental manifestation and corresponding numerical modeling of the DRS. Specifically, we fabricate a 3D-printed chain of HECs, and show that this nonlinear waveguide follows the strain-softening behavior with the nonlinear exponent $p < 1$, stemming from its geometrical nonlinearity. Using this 1D HEC chain, we demonstrate the emergence of the DRS under a striker impact condition. Furthermore, two of unique features of the DRS, i.e., the back-tilted wavefront due to the rarefaction and the oscillatory wave tails due to the dispersive shock, are validated not only experimentally, but also computationally by using the finite element and the discrete element methods. Ultimately, we assess the effect of wave dispersion and rarefaction by the DRS in comparison to the material damping effect, confirming the efficacy of the HEC in stress wave attenuation.

In Chapter 4, we numerically and experimentally verify the Bloch oscillations in the 3D-printed chain of hollow elliptical cylinders (HECs). We impose a linear gradient to the thickness of the HECs in the chain. 3D-printing provides an exceptional tunability in the design and fabrication of the HECs. With the power of 3D-printing, we can manufacture the HECs at desired thicknesses with high precision. The controlled thickness variation results in

the gradient in the contact stiffness [2], creating slanted frequency band structures. This can form a counterpart of the Wannier-Stark ladders for elastic waves. As a result, we observe the Bloch oscillations of the waves in the mechanical test bed. We show that the location of the Bloch oscillations depends on the excitation frequency due to the Wannier-Stark ladders. This enables the control of energy localization in solids for potential engineering applications.

In Chapter 5, we evaluate nonlinear wave dynamics in 3D-printed, graded lattices composed of HECs. The gradient in the geometry of the HECs along the chain results in the asymmetric dynamics of stress wave propagation. That is, the impact mitigating behavior in the positive gradient chain and that in the negative gradient chain are highly distinctive. The nonreciprocal wave propagation in nonlinear systems has been studied extensively, mainly relying on the multi-stability of their unit cells. For example, [76] have found a mechanical diode using bistable lattices. [77] have used multi-stable stacked-origami to realize a static mechanical diode effect. [78, 79] have recently reported unidirectional transmission of energy in metastable structures. However, the asymmetric dynamics in a nonlinear mechanical system without relying on multi-stability has been relatively unexplored.

We numerically and experimentally verify the impact absorbing mechanism of graded HEC structures in 1D as well as 2D architectures. In particular, we leverage the strain-softening nature of the HECs to demonstrate the asymmetric wave dynamics. The stiffness and the mass gradient combined with the strain-softening nonlinearity create the unique dynamics. These HEC lattices can be easily fabricated using 3D-printing and assembled by simple bonding, in sharp contrast to granular crystals which need delicate mechanical contact. This provides us the following advantages: First, we can avoid the issues regarding the energy dissipation due to the rotational and shear friction of granular beads in experiment. Second, we have the flexibility to design and the convenience to fabricate the unit cells. These advantages enable us to customize the unit cells to show various behaviors and investigate their effect on wave dynamics. Finally, we can achieve a low weight-to-volume ratio structure by using generic polymer materials as well as by optimally designing the structures.

In Chapter 6, we present preliminary study on impact response of 2D HEC array. We

change the aspect ratio of the unit HECs to explore how the dynamic response changes. Furthermore, we investigate the effect of the impact condition, i.e., striker mass and velocity. We combine these two parameters to visualize how they affect the wave dynamics within the 2D HEC array.

Chapter 2

LINEAR WAVE PROPAGATION IN 1D HEC

In this chapter, we briefly explore linear dynamics of the chain of hollow elliptical cylinders (HECs). We first numerically and experimentally examine force-displacement relationship of a single HEC unit cell. Second, we explore the dispersion relationship of the HEC chain. We investigate the frequency response of the HEC chain and compare it with the dispersion relationship.

2.1 Static analysis

2.1.1 Finite element analysis

We use commercial finite element method (FEM) software (ABAQUS) to conduct numerical simulations of static response of a single HEC cell and dynamic wave propagation in the HEC chain. We adopt a quadratic beam element (B22) for capturing deformation of the HECs. Also, this Timoshenko beam takes into account any transverse shear of the HEC during the simulations. For the constitutive relation of the FEM element, we use the Neo-Hookean hyperelastic model to account for the nonlinear polymeric material behavior of PLA in static regime. The strain energy potential for Neo-Hookean model is [80]

$$U = \frac{\mu}{2}(\bar{I}_1 - 3) + \frac{K}{2}(J_{el} - 1)^2 \tag{2.1}$$

where μ is shear modulus, $\bar{I}_1$ is first deviatoric strain invariant, K is bulk modulus, and J_{el} is elastic volume ratio. We assume incompressible material such that $K = 0$. $\bar{I}_1$ is defined as $\bar{I}_1 = \bar{\lambda}_1^2 + \bar{\lambda}_2^2 + \bar{\lambda}_3^2$ where the deviatoric stretches $\bar{\lambda}_i = J^{-\frac{1}{3}}\lambda_i$; λ_i is the principal stretches and J is the total volume change defined by the determinant of the deformation gradient. We

Some of texts and figures in this chapter have been partly taken from the author's publication [1].

find the shear modulus of the Neo-Hookean model in Eq. (2.1) empirically ($\mu = 515 \times 10^6$ N/m^2) based on the force-displacement curve that is obtained from the quasi-static loading test on the HEC (further details in Section 2.1.2).

2.1.2 Quasi-static compression test

We conduct compression tests on five different HEC prototypes along their major axis. We make sure that the compression speed is low enough to be considered in static regime. We use the strain rate of 0.1 mm/s (0.003 s^{-1}) which falls in the quasi-static regime and under which stress-strain behavior shows negligible difference [81, 82]. We plot the average force value with respect to displacement (blue curve in Fig. 2.1, where compressive force and displacement are plotted positive). The standard deviations among the data sets are also plotted in a lighter color.

We can find the Neo-Hookean constant μ that yields the least root-mean-square error compared to the experimental data ($\mu = 515 \times 10^6$ N/m^2). We observe that the FEM result and the experimental data are in good agreement up to 3 mm or 10% strain (red dashed line versus blue solid line Fig. 2.1). The strain range of interest (i.e., $\Delta x/a$ where Δx is displacement and a is the unit cell length) of this study does not exceed 2 mm under the considered range of dynamic impact, which safely falls within the 10% strain limit. One thing to note is that the force-displacement curve is nonlinear. Specifically, the slope of the curve decreases with increasing displacement. This nonlinearity stems from the geometry of the HECs being thin-walled tubes. Another thing to note is that the Neo-Hookean hyperelasticity models static behavior. At this stage, we are certain that the static behavior of the HECs follows the Neo-Hookean model. However, we will have to calibrate the material constant for dynamic analysis, which is discussed in Section 3.5.

2.1.3 Curve-fitting of the force-displacement relationship

In Fig. 2.1, we also plot a power-law fitted curve (brown solid line) [19] based on Eq. (3.2) in Section 3.3. This is essentially for dynamic analysis using discrete element method (DEM)

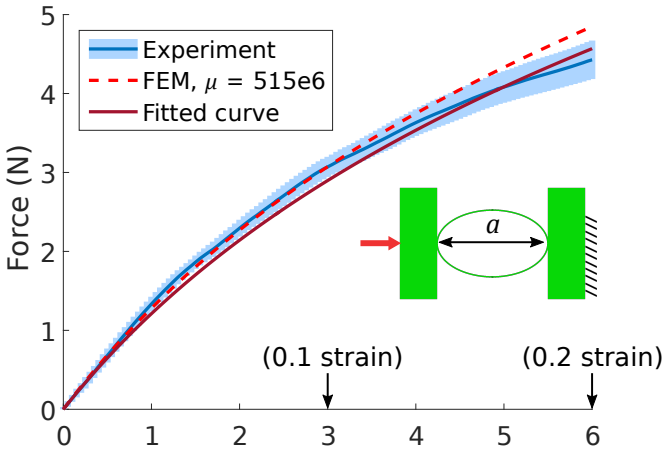

Figure 2.1: Compressive behavior of the HEC. Experimental results (blue curve) with their standard deviations (light blue area), the Neo-Hookean model-based FEM results (red dashed), and curve-fitting of the experimental data into a power-law relation (brown solid line). The inset is a schematic of the initial state of the compression test. A force is applied on the left panel (red arrow) whereas the right panel is fixed. $a = 30$ mm is the unit cell length. The strain is calculated as $\Delta x/a$.

in Chapter 3 but it is convenient to mention its validity while we are discussing the static analysis. The fitting process is as follows. We assume that the nonlinear springs that connect the lumped masses in the DEM follow a power-law relationship. The validity of this power-law assumption is well illustrated in Fig. 2.1, where it closely aligns with the experimental and FEM results. We discuss the plausibility of this model later in Section 3.6.1. Mathematically, this power-law relationship can be expressed as:

$$F = A(\delta_0 + \Delta x)^p - f_0, \tag{2.2}$$

where F is contact force, Δx is relative displacement of HEC centers, A is a contact constant, δ_0 is an effective pre-compression term, p is the relevant exponent, and f_0 is a balancing constant to make $F = 0$ at $\Delta x = 0$. Note that non-zero δ_0 needs to be introduced here, since without it, the initial stiffness of the force-displacement relation (i.e., $\dfrac{dF}{d\Delta x}$ at $\Delta x = 0$) becomes infinite when $0 < p < 1$. Thus, given the finite value of the linearized stiffness k_0,

	cylinder-cylinder	cylinder - wall
p	0.1817	0.4105
δ_0 (mm)	3.066	0.3793

Table 2.1: Curve-fitted contact parameters for different contact conditions.

we need to introduce the effective pre-compression term δ_0.

From Eq. (2.2), we can reduce the number of unknown parameters by applying proper conditions. Since the initial tangent should be the effective stiffness and there is no residual force in the chain,

$$\begin{cases} \left.\dfrac{dF}{d\Delta x}\right|_{\Delta x=0} &= Ap\delta_0^{p-1} = k_0 \\ F(0) &= A\delta_0^p - f_0 = 0 \end{cases}$$

$$\therefore \begin{cases} A &= k_0/p\delta_0^{p-1} \\ f_0 &= A\delta_0^p = k_0\delta_0/p \end{cases}$$

Now we have only two unknown parameters, p and δ_0, to fit in Eq. (2.2). We use *fmincon* module in MATLAB to process optimization based on experimental data to find the nonlinear exponent p and the effective pre-compression term δ_0. Note that the similar approach can be taken between the HEC and the PLA wall at the beginning and end of the chain. The resulting values are listed in Table 2.1.

2.2 Dispersion relation of the HECs

2.2.1 Calculation of dispersion relation

To examine the nature of the dispersion relation for the different bands emerging in the *infinite* HEC chain, we calculate the dispersion curves (Fig. 2.2) for the unit HEC in the irreducible Brillouin zone using ABAQUS. Here, we only consider the major axis direction and symmetric modes about the major axis. Figure 2.2(a) shows the dispersion curves with stop bands which is shaded in gray color. In Fig. 2.2(a), we have the cutoff frequency of the

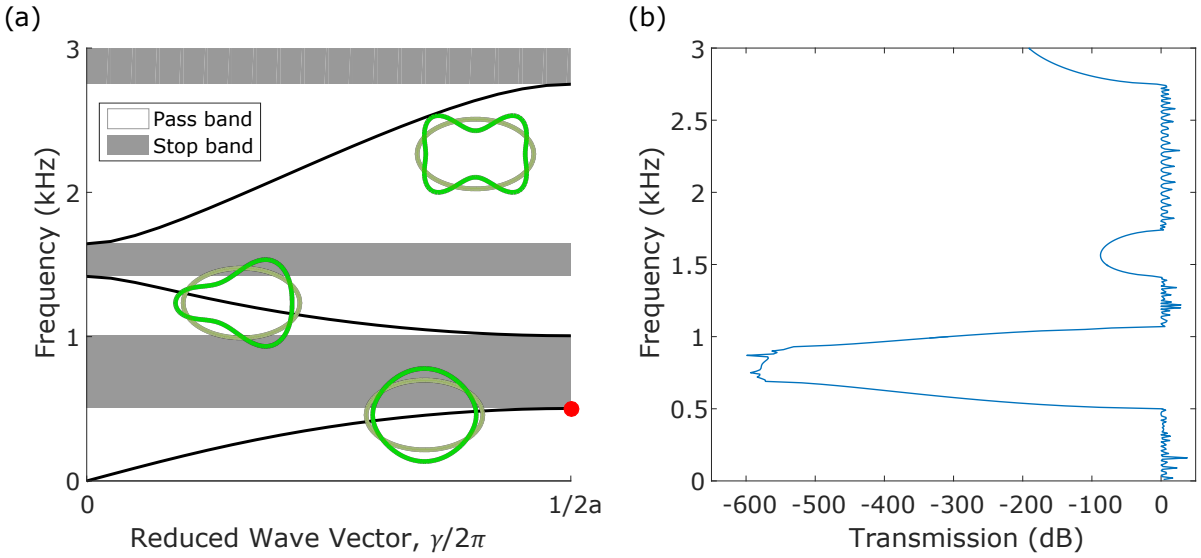

Figure 2.2: (a)Dispersion curve of one HEC by imposing infinite boundary condition. Only symmetric modes with respect to the major axis are presented. Red circle is where the cutoff frequency of the first mode is. The mode shapes are symmetric with respect to the minor axis in odd-numbered modes and asymmetric in even-numbered modes (see the insets for vibration modes obtained from the FEM). a is the unit cell length and γ is the wavenumber. (b) Transmission at the end of the chain at different frequencies.

first mode $f_c = 502.25$ Hz, which corresponds to the natural frequency of the HEC in its first symmetric mode. The first and the third mode correspond to the *symmetric* oscillations of the HEC, while the second mode is the *asymmetric* oscillations of the HEC (about the minor axis direction). It should be noted that the resonant modes appearing in the HEC system involve the nonlocal geometry of the HECs. In other words, unlike conventional multi-DOF DEM models showing the lowest mode driven by the smaller masses (local) attached to a bigger mass, the first resonant frequency of the HEC excites the entire body (nonlocal). Higher modes of vibration may give rise to interesting breathing behavior associated with the bands and gaps of this multi-band system. Given these aspects, exploring higher modes constitutes to a challenging yet particularly fruitful direction for future research in this system.

A monoatomic (single-band) chain is well-known to feature the dispersion relation [83]:

$$\omega(\gamma) = 2\sqrt{\frac{k_0}{m}}\sin\left(\frac{\gamma a}{2}\right),$$

where ω is angular frequency, γ is wavenumber, m is a single HEC mass, and a is the unit cell size. The cutoff frequency of the dispersive branch is found at $\omega\left(\frac{\pi}{a}\right) = 2\sqrt{\frac{k_0}{m}} = \omega_c$. Then we can find the effective stiffness of the spring, k_0, as

$$k_0 = \left(\frac{\omega_c}{2}\right)^2 m = \left(\frac{2\pi f_c}{2}\right)^2 m = (\pi f_c)^2 m \tag{2.3}$$

Note that this k_0 corresponds to the linearized value of the nonlinear spring that connects lumped massed in the DEM. We will return to this point for deriving the nonlinear power-law relationship among the HECs.

We compare the effective stiffness with the calculated value from the experiment. The mass of the HEC is $m = 0.456$ g from FEM. Then we can simply calculate k_0 from Eq. (2.3) as $k_0 = (\pi \cdot (502.25))^2 \cdot (0.456 \times 10^{-3}) = 1135.3$ N/m. We obtain the initial stiffness from the force-displacement curve (blue solid line in Fig. 2.1) by taking a tangent of the two initial data points which is $k_0 = 1412.593$ N/m. Although the experimental value is slightly bigger, it is within a reasonable range of error. This is probably because the actual HEC is not a single DOF system but rather a continuous ring. Also, it is possible that the viscoelasticity is in effect in the compression test. It could be interesting to explore strain-rate dependency of the 3D-printed HEC for future research.

2.2.2 Frequency response of the HEC chain

To verify the dispersion relation we obtain in Fig. 2.2(a), we conduct steady-state dynamic analysis using ABAQUS. We excite a HEC chain with the chain length of $N = 26$ from 1 Hz to 3 kHz. We measure the output velocity and calculate the transmission as $20\log_{10}\frac{v_{out}}{v_{in}}$ (dB) where v_{out} is the output velocity and v_{in} is the input velocity. We plot the transmission value with respect to the frequency in Fig. 2.2(b). It is clear that the low transmission

regions in Fig. 2.2(b) align with the band gaps in Fig. 2.2(a). We confirm that the number of HEC of $N = 26$ is enough to capture the linear dynamics of HEC system.

Chapter 3

NONLINEAR WAVE PROPAGATION IN 1D HEC

In this chapter, we report an experimental and numerical demonstration of dispersive rarefaction shocks (DRS) in a 3D-printed soft chain of hollow elliptical cylinders (HECs). We find that, in contrast to conventional nonlinear waves, these DRS have their lower amplitude components travel faster, while the higher amplitude ones propagate slower. This results in the backward-tilted shape of the front of the wave (the *rarefaction* segment) and the breakage of wave tails into a modulated waveform (the *dispersive shock* segment). Examining the DRS under various impact conditions, we find the counter-intuitive feature that the higher striker velocity causes the slower propagation of the DRS. These unique features can be useful for mitigating impact controllably and efficiently without relying on material damping or plasticity effects.

3.1 Experiment

The experimental setup is composed of a chain of HECs, a striker impact system, and measurement devices (Fig. 3.1). The chain consists of 26 HECs, which are 3D-printed (Ultimaker 3) with a poly-lactic acid (PLA) material and epoxy-bonded together at their interfaces. The mass of each HEC is $m = 0.455 \pm 0.006$ g. Two linear stainless steel shafts (diameter: 2.38 mm) penetrate the side surfaces of the HECs to align them and to restrict their lateral motions. The two shafts are supported firmly by the 3D-printed jigs to minimize their vibrations. We note in passing that the HECs in this horizontal setup interact with each other following the power law with $p < 1$, so-called strain-softening [19], which is confirmed by the quasi-static loading test (see the bottom inset of Fig. 3.1 and Section 2.1.2 for details).

The texts and figures in this chapter have been partly taken from the author's publication [1].

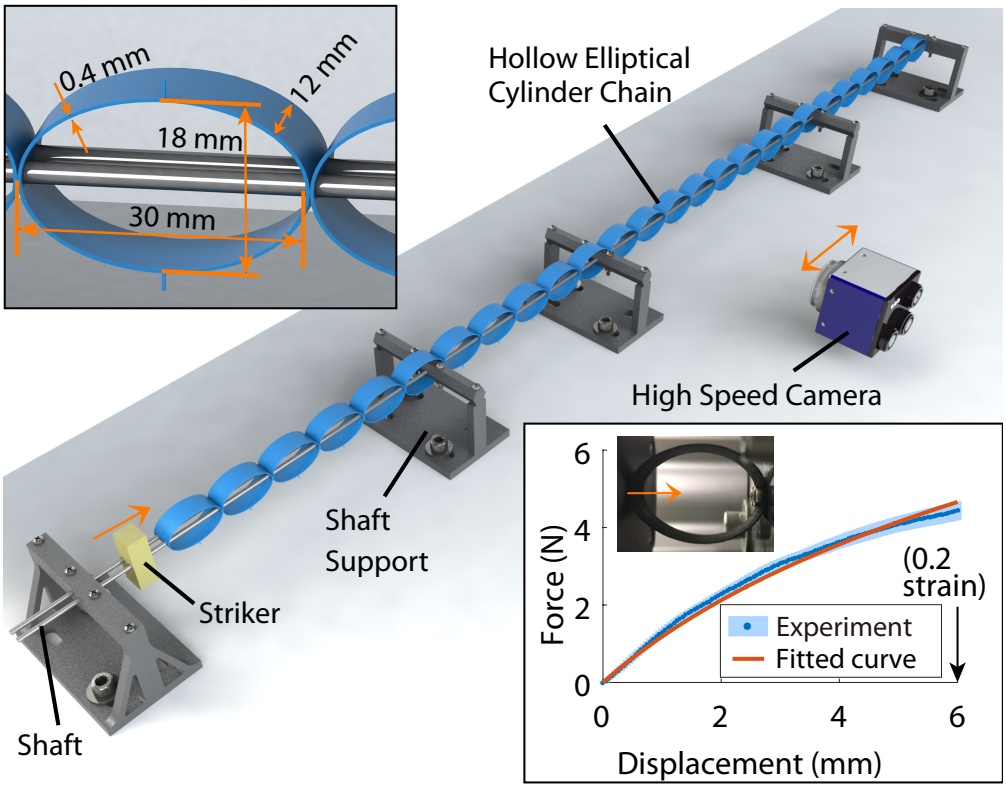

Figure 3.1: A schematic diagram of the dynamic test setup. The top inset illustrates the enlarged HEC unit cell and its dimensions. The bottom inset shows the force-displacement curve (blue) obtained from the quasi-static compression test, along with the power-law fitting result (red). The digital image shows the compression test setup. The compressive components of forces and displacements are defined positive throughout this chapter.

To apply impact to the HEC system, we use a vibration shaker (LDS V406, B&K) that launches a rectangular striker (PLA, mass: $m_s = 4.3$ g) towards the first HEC in the chain at a controllable and consistent speed ($v_s = 2.73 \pm 0.05$ m/s). The striker impact triggers the high speed camera (Phantom v1211) by means of a piezoelectric disc attached to the outer surface of the first HEC. The high speed camera is translated along the linear stage (BiSlide, Velmex) to capture the dynamic displacement profiles of each cylinder (i.e., x_n for the nth particle) by using the digital image correlation technique (show details in Section 3.5). In each measurement spot, we run the impact experiment five times for statistical treatment.

Based on the recorded displacements, the strain between neighboring particles can be obtained as

$$u_n = (x_{n+1} - x_n)/a \tag{3.1}$$

where a is the major axis length of the cylinder ($a = 30$ mm in this study). Figure 3.2(a) shows the surface map of the measured strains in space and time domains based on the experimental data, see Section 3.5 for details. A unique feature to notice is that the shape of the leading pulse changes from the initial compactly-supported shape to a wider one (see the increasing gap between the front edge (dashed line) and the peak points (dotted line) in Fig. 3.2(a). The change of the wave width from compact to wide support in the HEC system stems from the nonlinearity, which should be distinguished from the conventional wave dispersion in linear elastic media. Details on the backward-tilted shock formation are in [20]. This implies that the wave component with the smaller amplitude (i.e., front edge) travels faster than the one with the larger amplitude (wave peak). This results in the deformation of the waveform, such that it gradually leans backward and shifts the wave peak location to the rear. This is more evident from Figs. 3.2(d-f), where the shaded areas show the evolution of the wavefront shape in the space domain over time. These experimental results showcase the formation of the rarefaction wavefront. Another feature to take note of from Fig. 3.2(a) is that the wave shows oscillating wave trails whose peak amplitudes show a monotonic decrease [see also the trailing part of the wave in Fig. 3.2(f)]. This oscillatory pattern combining the amplitude-dependent wave speed with the dispersive phenomena is the principal characteristic of dispersive shock waves [84].

3.2 Numerical simulation

We also conduct numerical simulations of the DRS by using a finite element method (FEM) [Fig. 3.2(b), see Section 2.1.1 for details]. The formation of the DRS is also evident in the FEM results, and the DRS profiles based on the FEM are in agreement with the experimental results. The advantage of the FEM is that we can extend the chain length at will, so that we can observe the evolution of the DRS over a larger space domain, which, in turn, enables

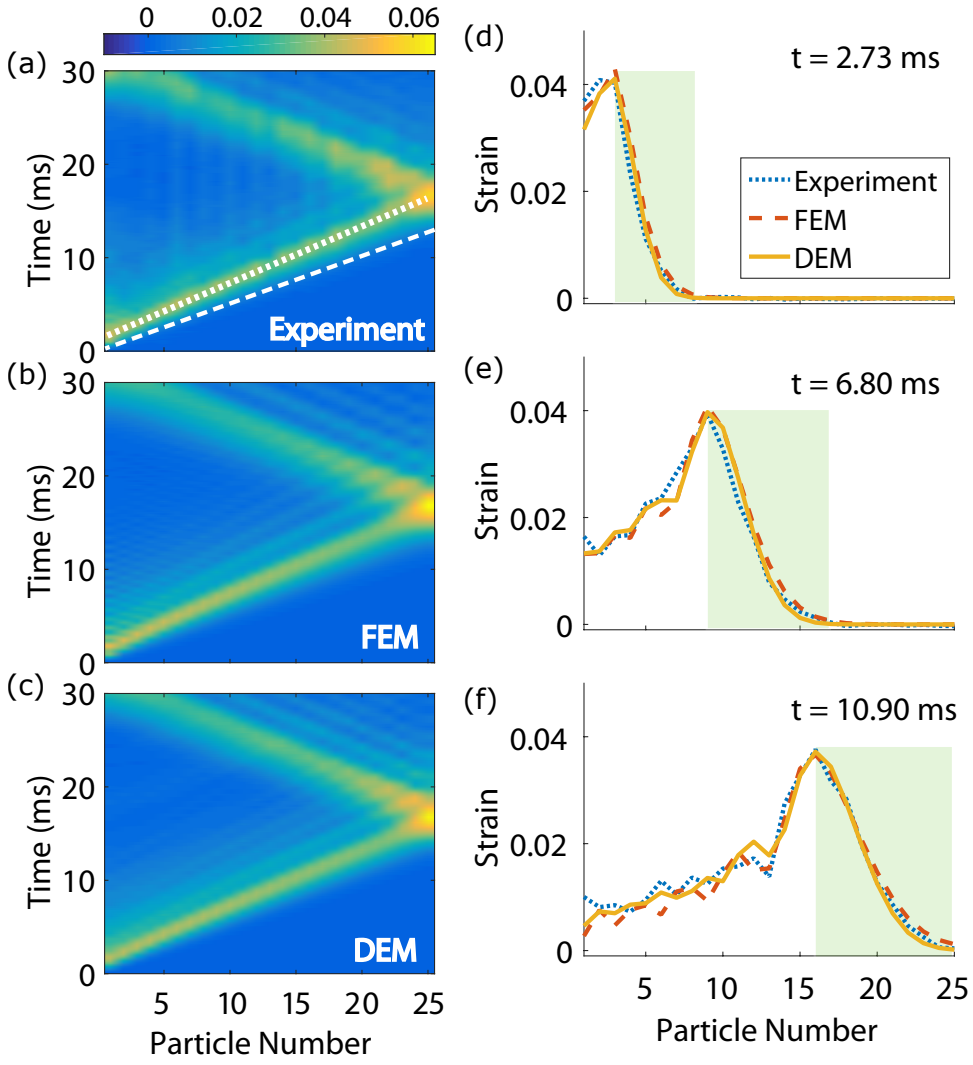

Figure 3.2: Surface map of strains in time and space domains from: (a) Experiments, (b) FEM, and (c) DEM. In (a), the white dotted line is the peak trace of the wavefront, and the white dashed line is its leading edge. Strain profiles are plotted at different time points, (d) $t = 2.73$ ms, (e) 6.78 ms, and (f) 10.88 ms based on experiments (blue dotted curves), FEM (red dashed curves), and DEM (yellow solid curves). The green shaded area denotes the enlarging spatial width of the DRS wavefront.

a more pronounced manifestation of the relevant phenomenology. Figure 3.3(a) shows the FEM simulation result of the spatial wave profiles of the DRS using an HEC chain with $N = 300$. First, we can clearly observe that the wave tail develops into a modulated waveform as the wave propagates through the HEC chain. This is strongly reminiscent of the multi-scale manifestation of dispersive shock waves [85]. In particular, the fast-traveling oscillatory waves which are harmonic when viewed in a local scale, bear an envelope of a slowly decaying modulation in a larger scale. Analyzing the frequency components in the wave tails, we find that they follow the local resonance of the HEC (see details in Section 3.6).

To complement the analysis, Fig. 3.3(b) shows the leading pulse profiles of the DRS, collected at different temporal moments but all aligned with respect to the origin in the space domain. It is evident that the wavefront width expands while its peak is attenuated. The evolution of the wave width is quantified in the inset in terms of the half-width-at-half-maximum (HWHM), which shows a monotonic increase. The experimental data points in hollow markers corroborate the FEM results for the short-chain region.

3.3 Discrete Element Method

While the FEM provides us with an accurate computational visualization of the experimental phenomenology, it would be beneficial to derive a simple yet effective model of the HEC chain. With a proper model capturing the principal features of the dynamics discussed herein, we can enhance our understanding of the forming mechanism of the DRS. To this end, we approximate the continuum HEC system via a 1D monomer chain of lumped masses based on the discrete element method (DEM). In this discrete system, the neighboring HEC particles are assumed to interact with each other by the following power-law [19]:

$$F = A(\Delta x + \delta_0)^p - f_0, \tag{3.2}$$

where A is the contact coefficient, Δx is the relative displacement between neighboring HEC centers, δ_0 is an effective pre-compression term, and f_0 is a force constant to incur no interactions under zero particle displacement (i.e., $f_0 = A\delta_0^p$). The validity of this power

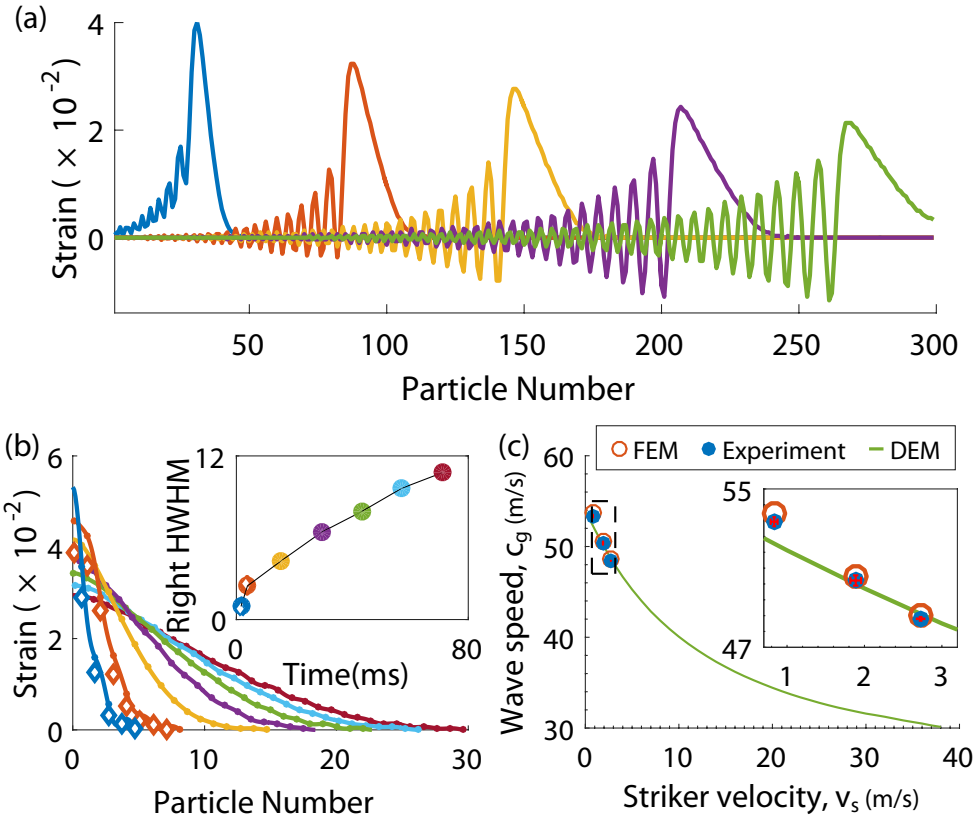

Figure 3.3: (a) FEM striker impact simulation result at $v_s = 2.73$ m/s, no damping included. The strain is calculated at time $t = 20$, 52, 84, 116, 148 ms from left to right. (b) The evolution of the leading pulse's waveform (right halves shifted to the origin) over time ($t = 1.7$, 3.9, 15, 29, 43, 57, and 71 ms from compact- to broad-supported shapes). The inset shows the right HWHM over time. The diamond markers denote experiment results. (c) c_g *vs.* v_s ($N = 26$). The green curve shows DEM simulation results, while the experimental and FEM results are shown in solid blue and hollow red circles, respectively. The inset shows an enlarged view around the experiment data points.

law in our HEC system is demonstrated by the curve fitting result shown in the bottom inset of Fig. 3.1 (further details for deriving the coefficients of Eq. (3.2) are in Section 2.1.3). We have confirmed that the present setting pertains to the weakly nonlinear regime (i.e., $\Delta x/\delta_0 \approx 0.4$) and that a power law approximation of the corresponding nonlinearity is suitable for representing the relevant phenomenology (Section 3.7.1).

For the nth particle in the HEC chain, the equation of motion can be written as

$$m\ddot{x}_n = A(\delta_0 + x_{n-1} - x_n)^p - A(\delta_0 + x_n - x_{n+1})^p - c_d\dot{x}_n, \tag{3.3}$$

where $n = 2, 3, \cdots, N-1$ ($N = 26$), the overdot denotes a time-derivative, and c_d is the damping coefficient obtained empirically by curve-fitting with the experimental data. To account for the boundary conditions, the equations of motions for the first ($n = 1$) and the last ($n = $ N) particles need to be modified (see Section 3.6 for details). We solve these differential equations using the fourth-order Runge-Kutta routine to analyze the dynamic response of the discretized HEC chain. Note that for the accurate comparison with the experimental results, we feed into the solver the first particle's displacement profile (i.e., x_1) obtained from the experiment. As a result, the strain surface map based on the DEM is plotted in Fig. 3.2(c). The DEM result is in good agreement with the experimental one [Fig. 3.2(a)]. The spatial profiles of the propagating DRS also corroborate those from the experiments and the FEM [Figs. 3.2(d-f)].

3.4 Amplitude dependent wave speed

By leveraging the fast and efficient computation of the DEM, we move on to the next question; as the striker velocity (v_s) is varied, how will the resulting DRS be affected as characterized by its group velocity (c_g)? Conventional nonlinear waves, including shocks, tend to generate faster traveling waves as we impose higher external excitations. For example, Nesterenko [8] derived the relationship $c_g \sim v_p^{1/5}$ in granular crystals, where v_p is the particle velocity that is directly related to v_s. Figure 3.3(c) shows the DEM calculation of c_g (green curve) as a function of v_s, where c_g is obtained by tracing the peak points in the strain map and

calculating their averaged slope [e.g., see the dotted-line slope of Fig. 3.2(a)]. Note that given the short chain ($N = 26$), the variation of c_g along the chain is less than 1%. In Fig. 3.3(c), it is striking that the leading pulse of the DRS propagates slower for higher external excitation in terms of the striker velocity applied.

To experimentally verify this important by-product of the strain-softening nature of the HEC chain, we conduct impact tests with various striker velocities: $v_s = 1.89 \pm 0.07$ m/s and $v_s = 0.83 \pm 0.04$ m/s, which are roughly 2/3 and 1/3 of the previous striker velocity. Their results are plotted in Fig. 3.3(c) in solid dots (see also the inset, where error bars based on the standard deviations of the five tests are almost invisible due to consistency). The numerical results from the FEM are also marked in red circular dots. We confirm that the experimental and computational results corroborate the negative correlation between v_s and c_g predicted by the DEM. We also note that at $v_s \approx 0$, we have $c_g \approx 54$ m/s, which corresponds to the linear wave (i.e., sound wave) speed in the HEC chain. Becasue of this asymptotic nature of c_g, we find that the relationship between the group and phase speeds does not follow the aforementioned power law of $c_g \sim v_p^{1/5}$ shown in the typical granular chains (see Section 3.7.2 for details).

To assess the efficacy of the HEC chain as an impact mitigation system, we calculate the evolution of the maximum potential energy experienced by each inter-particle location, as the wave propagates along the chain. The potential energy $\Psi(n)$ stored in the nth inter-particle spot can be simply found by integrating Eq. (3.2) as

$$\Psi(n) = \frac{A}{p+1}\left[(\delta_0 + x_n - x_{n+1})^{p+1} - \delta_0^{p+1}\right] - f_0(x_n - x_{n+1}).$$

We calculate the potential energy over time and find a peak value, $\Psi_{\max}(n)$, in each inter-particle location. This potential energy value after normalization[1] is shown in Fig. 3.4. The solid curve denotes the DEM results based on the curve-fitting with the experimental data (see diamond dots with error bars in the inset). In this process, the degree of the

[1]We normalize the potential energy by dividing the $\Psi_{max}(n)$ by $\Psi_{max}(1)$. For DEM model, however, we use $\Psi_{max}(2)$ as a denominator since the initial strain exceeds the one from the experiment.

material damping - in terms of the chain damping coefficient c_d (in Eq. (3.3)) and the striker damping coefficient c_s (see Section 3.6.2-3.6.3) - is optimized, such that the DEM best fits the experimental trend. We observe the fast decay of the peak potential energy over the spatial regime, which manifests a highly efficient mechanism of stress wave attenuation in the HEC system.

It is now natural to inquire about the portion of this attenuation contributed by the combined dispersion and rarefaction mechanism in the DRS, compared to the material damping effect. This question can be answered by assessing the effect of the material damping on the overall wave attenuation. For this, we run the DEM simulation with zero damping coefficients. The results are shown in the dotted curve in Fig. 3.4, which also shows a rapid drop of $\Psi(n)$ over the space. Comparing the two DEM cases (i.e., solid and dashed curves), the energy reduction from the non-damped to the damped DEM results is 19.3% over the span of 250-particle chain. However, the potential energy drop even for the non-damped case is around 76.8% at the end of the chain, compared to the initial energy level. This implies that the wave attenuation solely due to the combined dispersion and rarefaction is more than three times larger than that due to the damping in the given system. Though the relative portions can change depending on the system configurations, size, and boundary conditions, this trend overall supports that the formation of the DRS can be an efficient way of mitigating stress waves without resorting to material damping or plasticity effects.

3.5 Methods

We fabricate the HECs and conduct the dynamic test on the HEC chain by applying compressive impact to the system. We use a 3D printer (Ultimaker 3) to fabricate the hollow elliptical cylinders (HECs). The HECs are made of a Poly-lactic Acid (PLA) material (Ultimaker), and the printing layer resolution is set to 0.06 mm. We prevent the warping of the HECs at the bottom rim by increasing the build plate temperature to 61 °C instead of printing the build plate adhesion which can cause irregular cylinder thickness when we take it off from the cylinders. The HECs are bonded with each other at the contact areas with

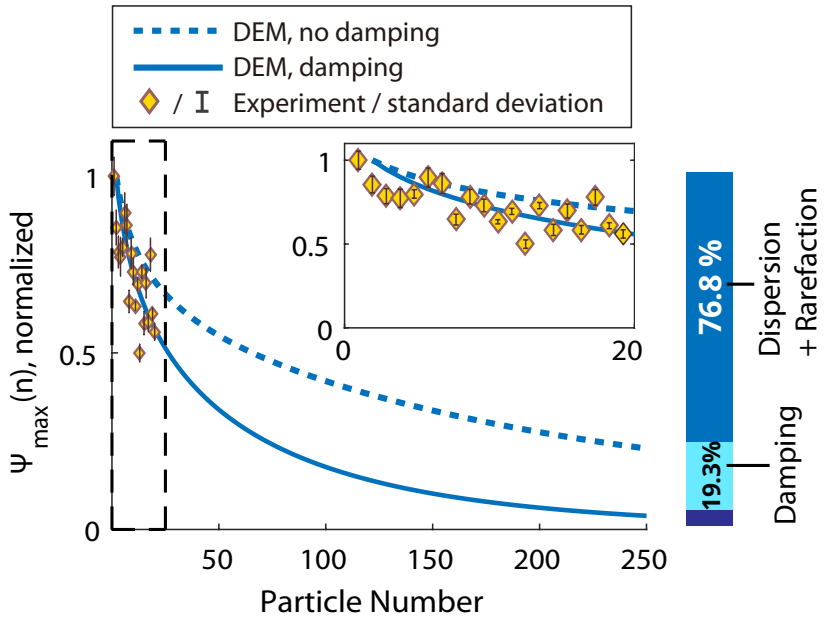

Figure 3.4: The peak potential energy for each cylinder, normalized by the input potential energy, is plotted as a function of the inter-particle location. Solid and dotted curves represent the DEM results with and without damping, respectively. Experiment results are plotted as yellow diamonds in the beginning of the chain, which can be more clearly seen in the inset. The bar graph on the right shows the contribution of the damping (cyan) and the combined effect of dispersion and rarefaction (blue) to the overall potential energy reduction (in case of $c_d = 0.003$ and $c_s = 0.2$).

super glue (Loctite 431) to prevent separation.

We send a step input signal to the shaker (LDS V406 M4-CE, Brüel & Kjær) such that the striker pushed by the shaker head reaches the desired speed at the impact to the chain. We use a piezoelectric ceramic disk (STEMiNC, 5x0.2 mm) to sync the impact incident and the beginning of video recording in every experiment. This piezoelectric actuator generates voltage signals up on the impact applied to the chain, which in turn triggers the high speed camera for data acquisition at 40 kHz sampling frequency and 2048-by-416 pixel resolution. We can see the piezo disc in Fig. 3.5(a), attached on the outer surface of the first HEC in the chain ($n = 1$).

We implement a digital image correlation (DIC) technique [86] to obtain the displacement of the HECs. For easy tracing of each particle's motion, we add a small marker in the center of the rim (Fig. 3.5(a)) when printing cylinders. For example, the trace of three green dots – representing the displacements of the first three particles, x_1, x_2, and x_3 – are plotted in Fig. 3.5(b) as a function of time. Based on these displacement profiles of each cylinder, we calculate the strain variable between neighboring cylinders (Fig. 3.5(c)), defined as Eq. (3.1) in Section 3.1. The raw profiles of the strains for all particles over five measurements are shown in Fig. 3.5(d). We note that despite the irregularities in some profiles, the overall trend of stress wave propagation through the HEC chain is evidently observed.

As explained above, we capture the dynamics of the HEC system by keeping track of the central node of each HEC (i.e., green dots in Fig. 3.5(a)) via the DIC technique. In passing here, we need to verify whether these central nodes well represent the cylinders' movements. We use the FEM to compare the results of tracking the center of mass of the cylinder and the central node. When plotted together the strain value based on the center of mass and that on the central node are almost identical (Fig. 3.6). The difference between them is around 3.5% at maximum, but mostly the error remains less than 0.5%. All the results in Chapter 3 are conveniently based only on the central node in both experiments and FEM results.

Given that we observe qualitative agreement between the FEM and experiment, both showing DRS, we adjust the simulation parameters to quantitatively match the experimental

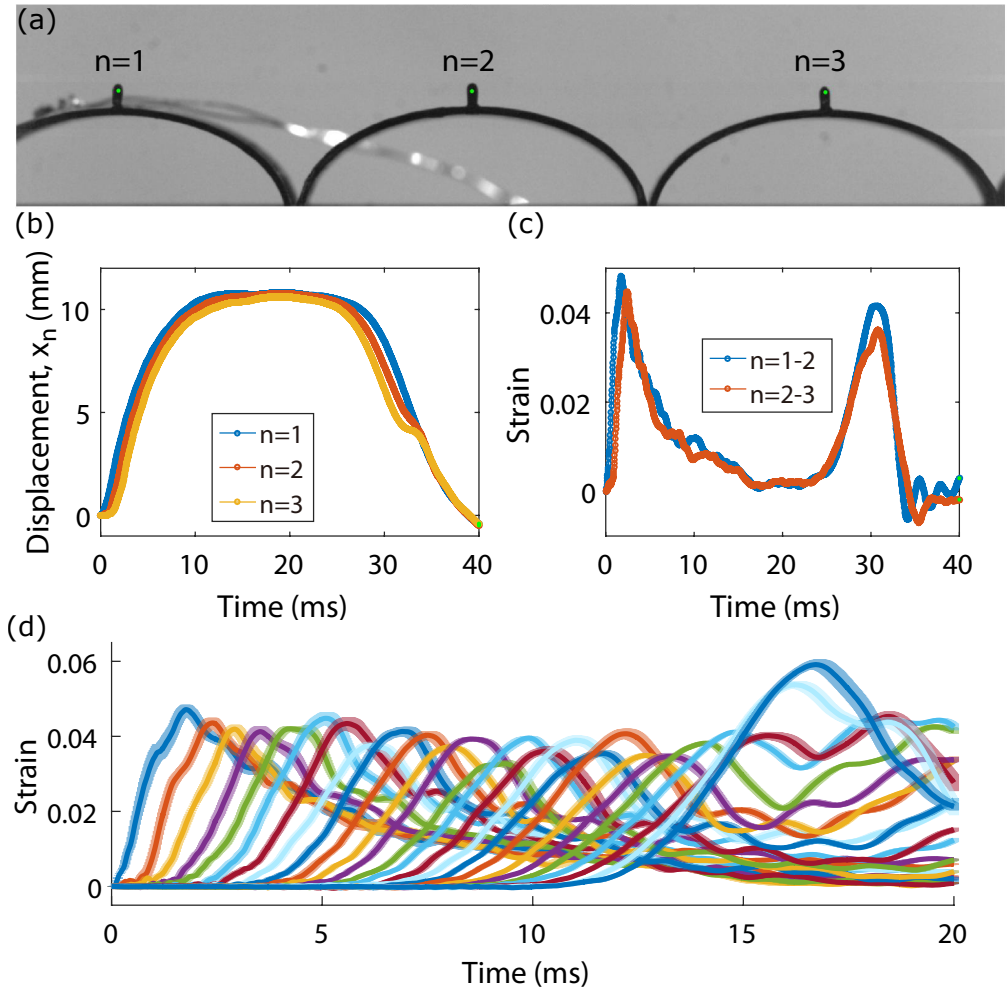

Figure 3.5: (a) A still cut image from the DIC process. Tracking the green dot on the markers yields the acquisition of the displacement profiles of each cylinder. (b) The result of displacement tracking of the first (blue circles), the second (red circles), and the third (yellow circles) cylinder using DIC technique. (c) Strain is calculated between the first and the second cylinder (blue circles) and between the second and the third cylinder (red circles). (d) Measured profiles of the strains for the HEC chain.

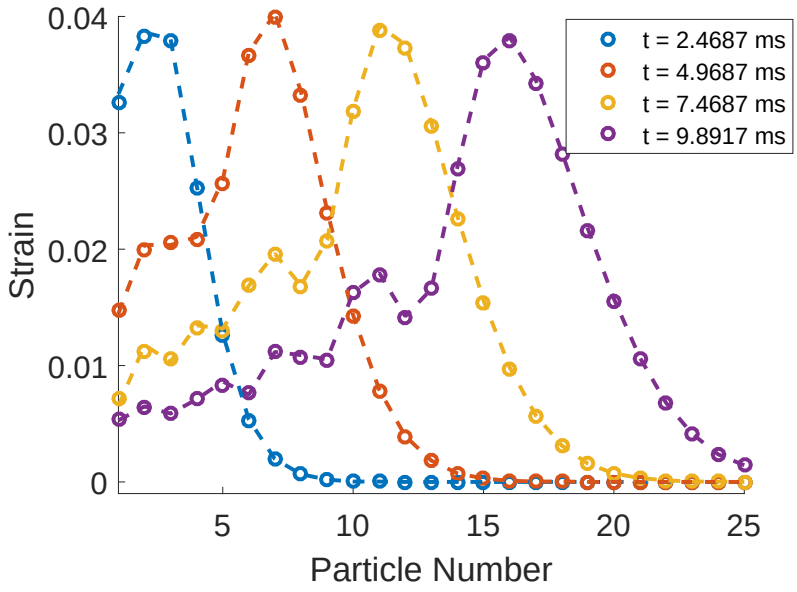

Figure 3.6: Wave propagation in spatial domain plotted based on the center of mass (circular markers) and based on the central nodes (dashed curves).

result. Here, we need to tweak two parameters: material constant and damping coefficient. As discussed in Section 2.1.2, we should adjust the material constant of the Neo-Hooekan model in dynamic analysis. Neo-Hookean model predicts static behavior, which means that it does not account for the effect of strain rate. Generally speaking, the material constant, μ, is responsible for the wave speed and the damping coefficient is responsible for attenuation. However, since the wave speed depends on the amplitude of the wave, these two are coupled. We follow the procedure reported in [87] to find the parameters, which is decribed in detail in Section 3.6.3. The material constant $\mu = 580 \times 10^6$ N/m^2 and the material damping coefficient $\alpha = 30$.

3.6 Equation of motion

3.6.1 Approximation to the 1 degree-of-freedom system

In the discrete element model (DEM) built in this study, we approximate the continuum HEC system into a 1D chain of lumped masses connected by nonlinear springs. That is, each HEC particle is reduced to a single degree-of-freedom (DOF) particle. Here we briefly justify this approach.Figures 3.7(a) and (b) show the 2D fast Fourier transformation (FFT) results of the strains obtained from the experiment and the FEM, respectively. The first two bottom branches in Fig. 2.2(a) match the ones observable from the experiment and FEM (Fig. 3.7(a) and (b)). While we observe signatures of the higher dispersive branches, we find that the main propagating wave is dominantly governed by the first mode (i.e., the bottom branch in red color). As discussed in Fig. 2.2(a), this first mode corresponds to the *symmetric* oscillations of the HEC, while the higher branch that we witness in Fig. 3.7(a) and Fig. 3.7(b) is due to the *asymmetric* oscillations of the HEC. The excitation of this asymmetric mode happens right after the incidence of the impact, as shown by the FFT result of the strain component u_1 at the beginning of the chain [Fig. 3.7(c) for the FFT results and Fig. 3.7(e) for raw signals]. However, as we can see from Fig. 3.7(d), the main mechanism of the wave propagation in the later part of the HEC chain relies on the first symmetric mode [raw signals in Fig. 3.7(f)]. In other words, when the impact is applied to the chain, multiple modes of vibration are excited. However, in the latter part of the chain, the main mechanism of wave propagation is through the vibrations of the base symmetric mode. To capture this base mode only, a 1-DOF model will suffice, and thus, we can justify the approximation of the HEC chain by a 1-DOF spring-mass system.

3.6.2 Modification of equations of motion for the DEM at the boundaries

In Section 3.3, we introduced the equations of motion for the HEC particles in the chain (see Eq. (3.3) in Section 3.3). This equation needs to be modified for the striker, the first particle, and the last particle in the chain due to the unique boundary conditions. Here we

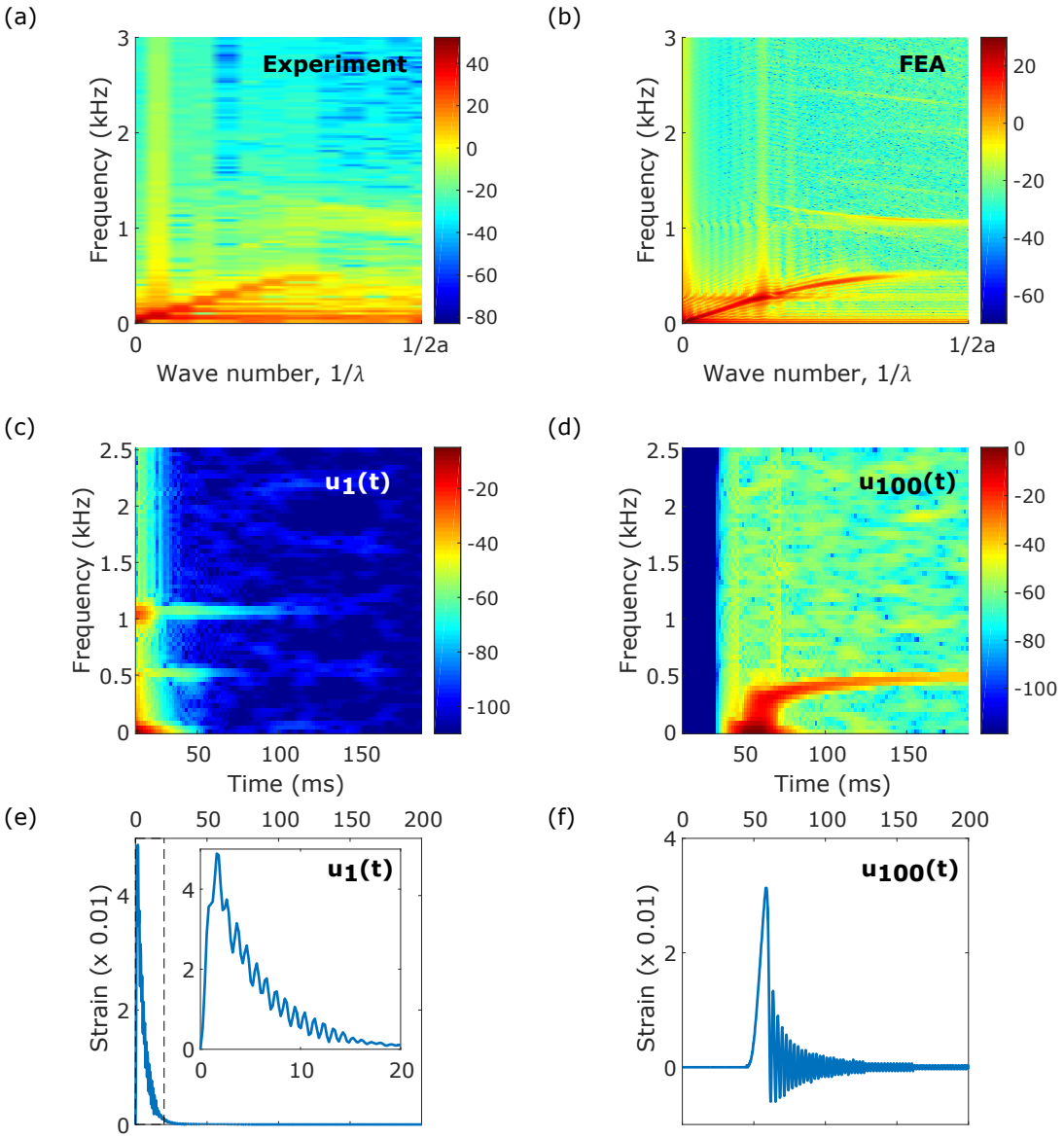

Figure 3.7: 2D fast Fourier transformation (FFT) on strain data (a) from the experiment results and (b) from the FEM simulation results of the long chain ($N = 300$) with no damping included. The short time FFT of the first cylinder strain obtained from FEM [$u_1(t)$ which is shown in (e)] is plotted in (c). Likewise, the short time FFT of the 100th cylinder strain from FEM [$u_{100}(t)$ as shown in (f)] is shown in (d).

elaborate on the details. First, the striker boundary condition (corresponds to $n = 0$) is as follows:

$$m_s\ddot{x}_s = -[A_s(\delta_{0,s} + [x_s - x_1]_+)^{p_s} - f_s] - c_s\dot{x}_s,$$

where subscript s denotes the quantities related to the striker. The bracket with sub-plus sign means that there is no interaction when there is no contact, i.e., $[x_n]_+ = \max(x_n, 0)$. Similarly, for the first and the last particles ($n = 1$ and $n = N$) in the chain,

$$m\ddot{x}_1 = (A_s(\delta_{0,s} + [x_s - x_1]_+)^{p_s} - f_s) - (A(\delta_0 + x_1 - x_2)^p - f_0) - c_d\dot{x}_1$$

$$m\ddot{x}_N = (A(\delta_0 + x_{N-1} - x_N)^p - f_0) - (A_w(\delta_{0,w} + [x_N]_+)^{p_w} - f_w) - c_d\dot{x}_N \tag{3.4}$$

where w is the subscript for the wall. The coefficients for the striker and the wall are the same since we are using the same PLA material. The coefficients are obtained by the empirical curve fitting, similar to the process for the identification of the parameters for the HEC particles, as explained in the previous section. Note that we only need the wall boundary condition in Eq. (3.4) for the short chain ($N = 26$) simulation because we use the first cylinder displacement (x_1) data obtained from the experiment. However, we do not have the x_1 information for the long chain ($N = 300$) and need all three aforementioned boundary conditions.

3.6.3 Finding damping parameters

Also, the damping parameters are obtained such that the dynamic analysis results from the DEM best match the experiment results. We follow the detailed procedure which can be found in the supplementary document of [87]. Briefly, we plot the strain wave at a few time points all together in space domain. Then we take the envelope of the profile (red circles in Fig. 3.8). Every time we run the simulation, we take the envelope the same way (red cross markers in Fig. 3.8) and calculate the error sum of the envelope points. We find the damping coefficients that minimize this error by performing the optimization technique.

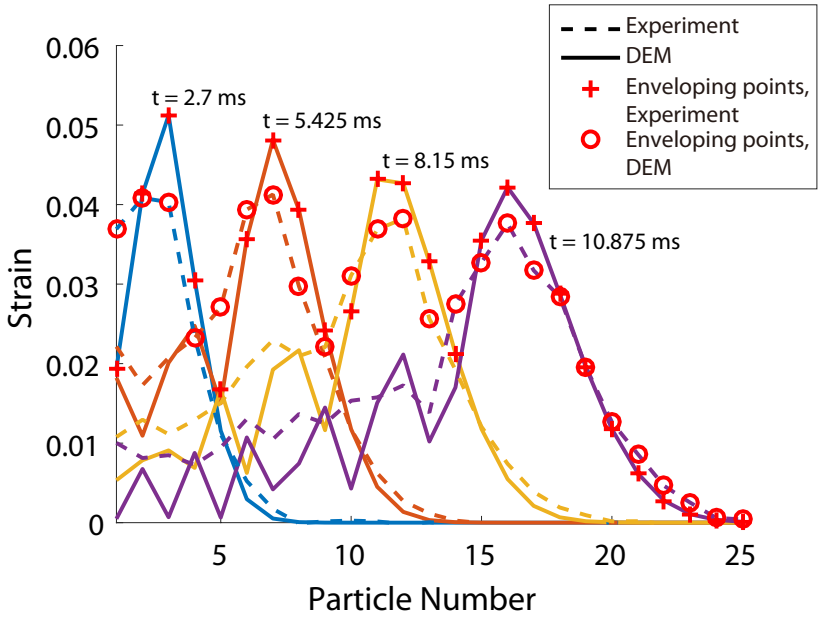

Figure 3.8: Strain wave propagation in space. The experimental results (dashed lines) and the DEM results (solid lines) are plotted at time t = 2.7 ms, 5.4 ms, 8.2 ms, and 10.9 ms from left to right. The red circles on the experimental results are points of reference while the red crosses are those to be fitted to the red circles.

3.7 Additional discussion

3.7.1 Verification of nonlinearity of the HECs

One fundamental question that can be raised in this study is whether the wave dynamics that we observe is truly nonlinear or not. To answer this question, we can start from explaining the nature of nonlinearity intrinsic in the HEC system. Then, we will move to the comparison of wave dynamics observed in our system with that in the purely linear case.

First, let $d_{\max} = |u_{i-1} - u_i| \approx 1.2$ mm be the maximum displacement during the shock wave propagation based on experimental observation. Judging from the near-linear trend within $d_{\max}$ in Fig. 2.1, one might doubt the nonlinear nature of the system. However, if we take a closer look around the point $d_{\max}$ in Fig. 3.9(a), we clearly witness the deviation between the linear approximation (black solid line taken from the initial slope) and the actual experimental response of the HEC prototype (blue circular dots). This clearly indicates that our HEC shows geometric nonlinearity in the range of its deformation considered in this study. This is more evident if we look at the stiffness change over displacement. In Fig. 3.9(b), we plot the stiffness of the system based on the slope of the force-displacement curve from Fig. 3.9(a). The variation in the stiffness reaches as much as 23.8% from the linear response of the HEC. Such decrease in stiffness within the range in experiments supports the intrinsic nonlinearity in the system.

The nonlinearity of our system is more obvious when we compare its dynamics with a linearized model as shown in Fig. 3.10. We use $k_0 = pA\delta_0^{p-1}$ for the linearized stiffness, while suppressing any nonlinearity in the force between the HEC units. In this linearized case (Fig. 3.10(a)), we see the propagation of the leading pulse followed by the wave oscillations in the tail, which is somewhat similar to the trend that we observe in the nonlinear case (Fig. 3.10(b)). If one compares these two cases closely, however, the leading pulse in the linear case does not undergo a noticeable change of the waveform (i.e., rarefaction characteristic) compared to the nonlinear case.

More evidence that this wave is a nonlinear shock wave is encompassed in the supersonic

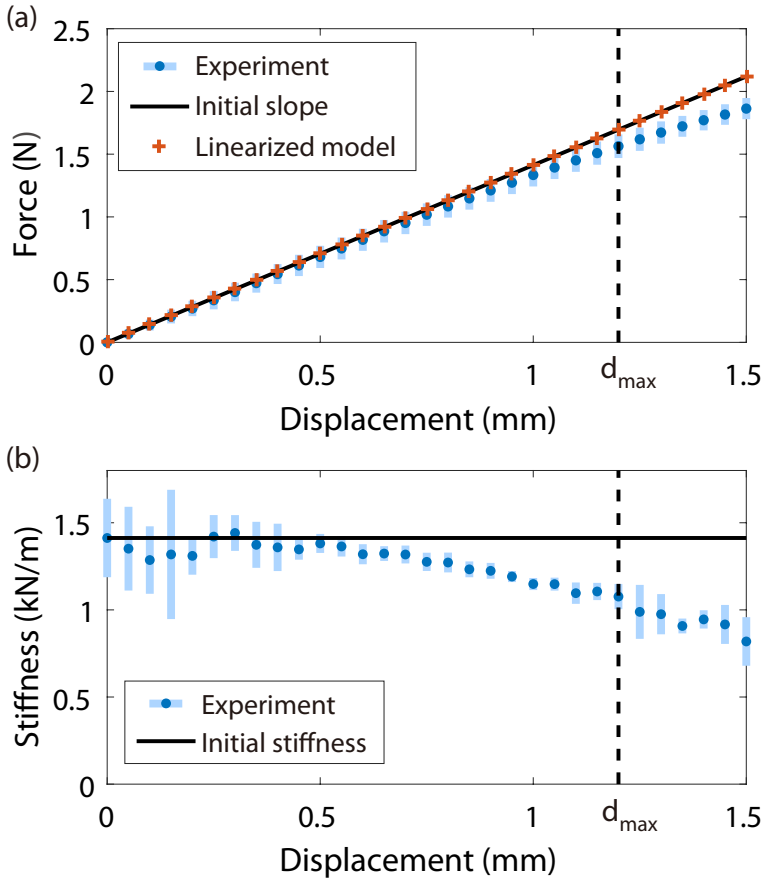

Figure 3.9: (a) Force-displacement from the compression test, reprinted from the bottom inset in Fig. 1 but for a smaller displacement range. The initial slope of the curve is extended and plotted as the black solid line. The linearized model is plotted in the orange cross markers. (b) Stiffness-displacement curve where the stiffness is calculated from the experiment data in (a). The initial stiffness, i.e., the initial slope in (a) is plotted in the black solid line to clearly show the decreasing stiffness of the HEC. In both plots, the light blue bars indicate the standard deviation from the five tests.

nature of the leading pulse observed in the nonlinear case. The group velocity of the leading pulse in the linear case is equal to the sound of speed. However, the group velocity of the leading pulse in the nonlinear case is 13.8% faster than the sound speed, confirming the supersonic propagation of the DRS. Observing the wave tails, we also find key differences between the two cases. Compared to the linear case, the nonlinear DRS tails clearly show fast-traveling oscillatory waveforms enclosed by a slow-decaying envelopes. As noted in Section 3.1-3.2, this multi-scale modulation is the manifestation of the dispersive shock waves. Lastly, the amplitude-dependent wave speed as depicted in Fig. 3.3(c) in Section 3.4 is another signature of nonlinear wave dynamics in the HEC system.

3.7.2 Group velocity and phase velocity

In order to investigate the relationship between the group velocity and the particle (phase) velocity, we run DEM simulations for an even longer chain ($N = 1000$). We can see in Fig. 3.11 that the wave speed increases as the particle velocity decreases. Furthermore, as the phase velocity decreases, it asymptotically approaches a constant value, which is the sound speed of this model. This behavior does not follow the power law $c_g \sim v_p^{(p-1)/(p+1)}$ (where p is the nonlinear exponent), which is the generalization of the predicted power law for the strain-hardening system that is derived in [8]. In other words, unlike the conventional granular chain showing "sonic vacuum" at very small particle velocities, the HEC chain delivers waves at finite speed which depends on the initial slope of the force-displacement curve.

3.7.3 Solitary waves in HEC

So far in Chapter 3, we have discussed dynamics of the HEC chain under heavy striker impact. A striker whose mass is far bigger than the unit cell generates a long input, resulting in a shock wave [88]. In our HEC chain, we observe a rarefied wave front and oscillatory wave trails, so called dispersive rarefaction shock (Refer to Fig. 3.2).

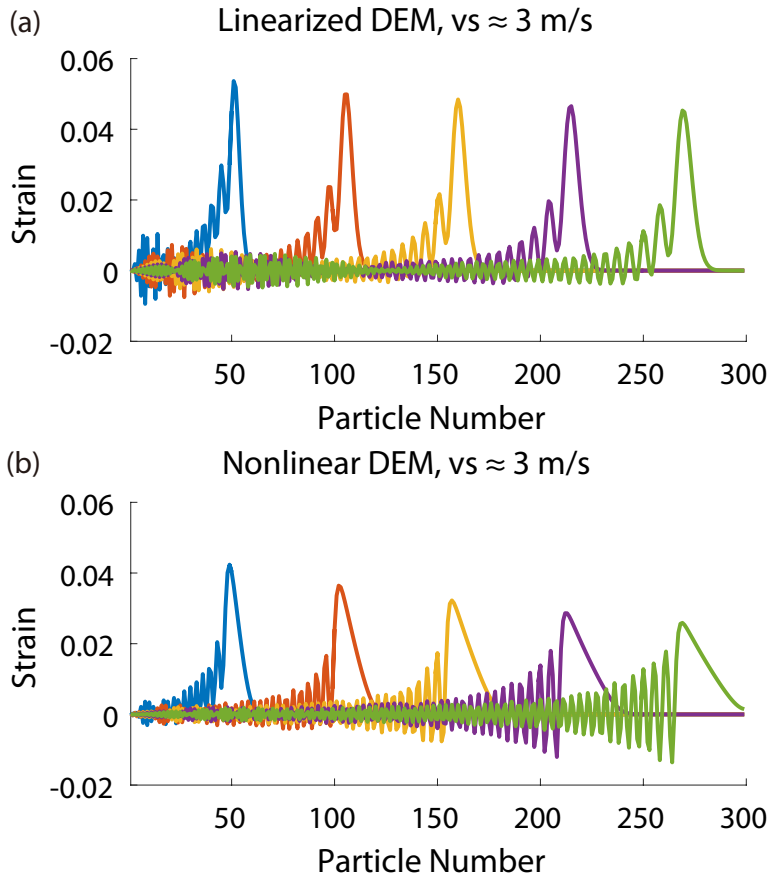

Figure 3.10: DEM simulation results with a striker impact at $v_s = 2.73$ m/s (a) using the linearized model captured at $t = 35$, 70, 105, 140, 175 ms and (b) the nonlinear model captured at $t = 31$, 61, 92, 123, 153 ms.

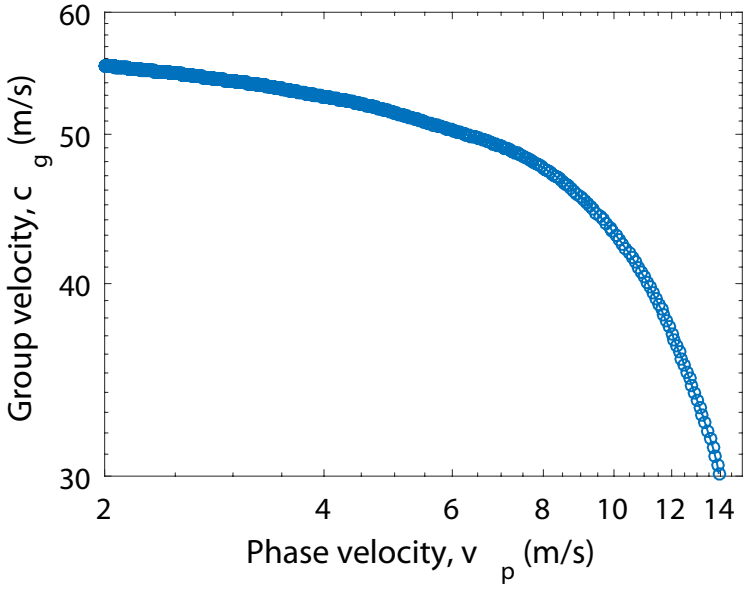

Figure 3.11: For DEM modeling of $N = 1000$ chain, the group velocity is plotted with respect to the phase (particle) velocity in log-log scale. The group velocity expression in space is obtained by using the polynomial curve-fitting method and is plotted with respect to the maximum particle velocity at each cylinder.

However, if we use a striker which is identical to the unit cell, we achieve a totally different response, a solitary wave. Solitary wave is highly localized in time such that it maintains its shape, undisturbed. To realize it, we also allow separation between HECs. Figure 3.12(a) shows the wave propagation in the HEC under a light striker impact. The schematic on the top illustrates the configuration of the chain. One thing to notice is that we do not see the oscillatory tail. Since the striker is so light, it applies a short input, which does not have the effect of compression of the chain. In addition, the HECs are separated, which means they cannot carry tensile waves. These two facts contribute to the solitary wave propagation. We notice that the wave front tends to expand, as we see in Fig. 3.12(b). However, it is not as significant as we observe in Fig. 3.2. Hence, we realize pseudo-solitary wave in the HEC chain under the light striker impact.

Next, we investigate the wave propagation along the minor direction under the light striker impact. The chain is roughly illustrated on top of Fig. 3.12(c). We arrange the HECs along its minor direction and apply an initial velocity to the first HEC. As seen in Fig. 3.12(c), the wave is highly localized in time domain, maintaining its temporal width as it travels. We see marginal expansion in the width and oscillations in the time lapse plot (Fig. 3.12(d)). It is notable that the wave front rather keeps its slope without expanding. This is one evidence that the HEC system becomes strain-hardening.

In fact, the configuration in the minor direction is merely a compressed state of the HEC along the major direction. We calculate the contact force and displacement relationship using FEA static analysis. Figure 3.13(a) shows the force-displacement curve along the major axis and (b) shows that along the minor axis. As we have already observed in the inset of Fig. 3.1 in Section 3.1, the initial part of the curve shows strain-softening. However, as the displacement reaches around 15 mm, it changes into strain-hardening. Moreover, we superimpose the force-displacement curve in the minor direction (orange dashed line) in Figure 3.13(a). The minor axis length is 18 mm which is 12 mm deformation in the major axis which is 30 mm. We translate the minor force-displacement curve to the corresponding point to compare with the major curve. We can see that they align very close to each other.

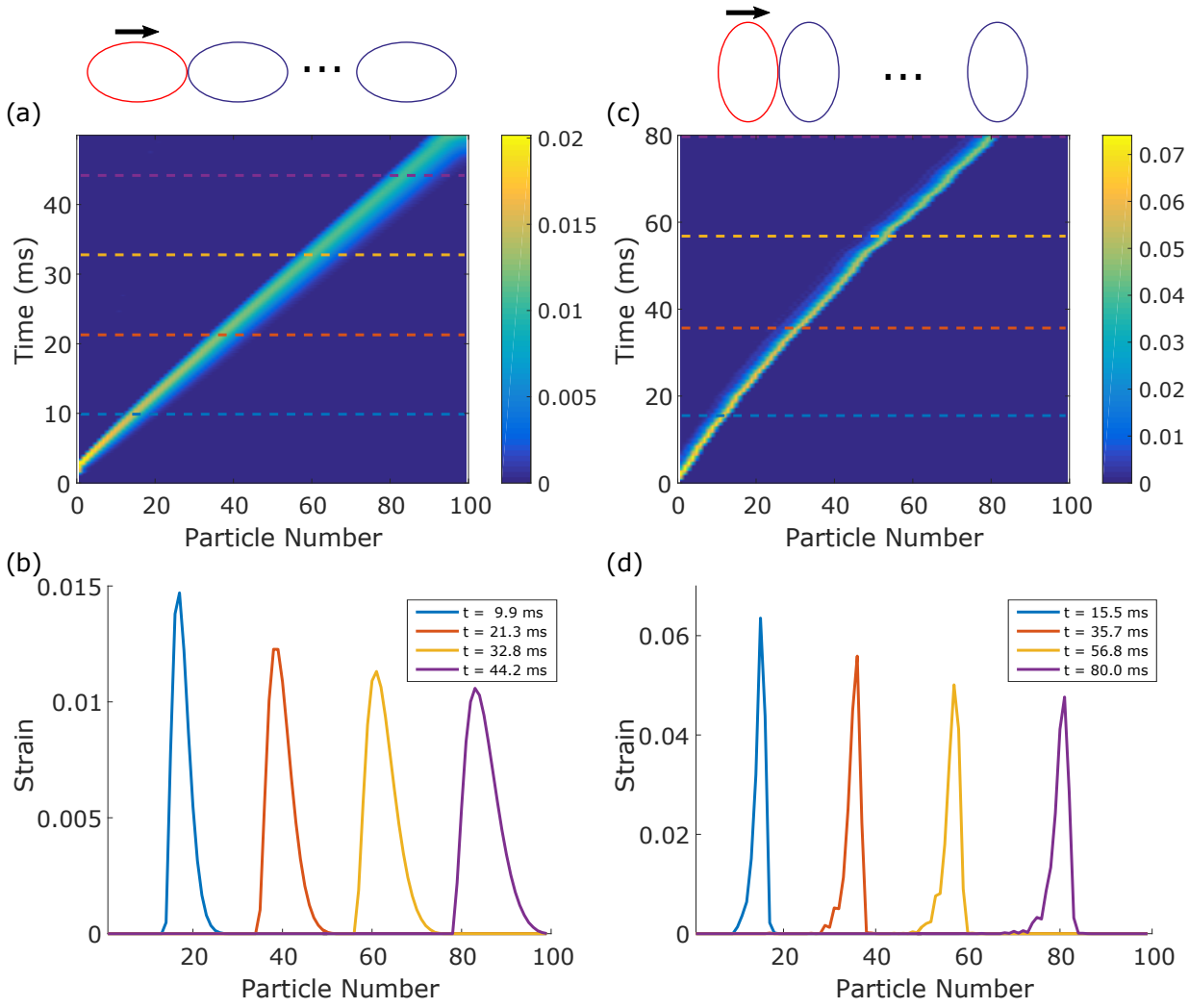

Figure 3.12: Contour map of strain of the HEC chain impacted by an identical unit cell (a) along the major axis (b) and its time lapse. Similarly, we plot (c) the spatial-temporal strain contour along the minor axis (d) and its time lapse. The schematics on top of (a) and (b) show the striker (red color) and the HEC chain. The dashed lines in (a) and (c) correspond to the time laps in (b) and (d), respectively. The lines are color-coded.

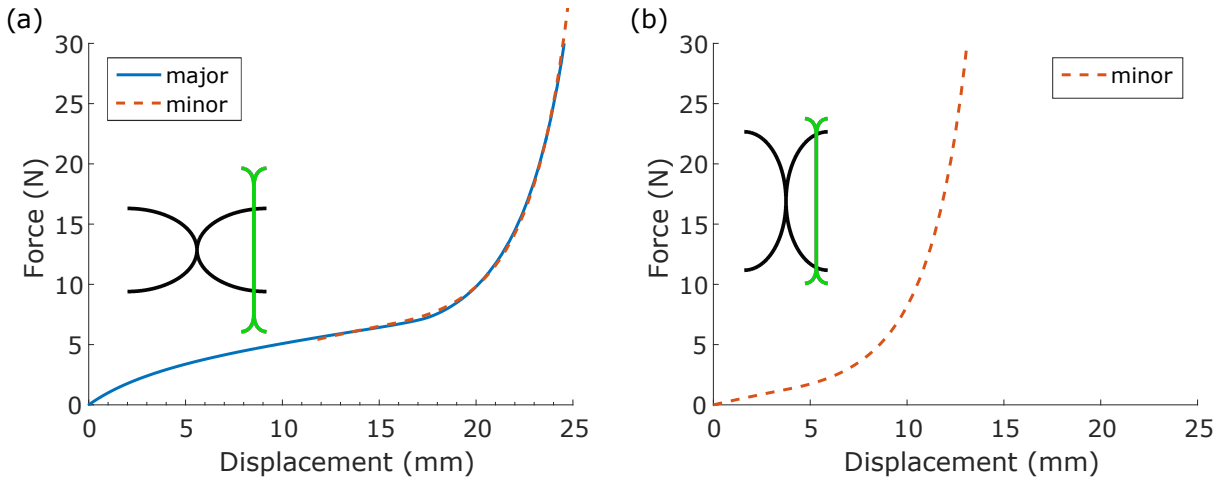

Figure 3.13: Force-displacement curve along (a) the major axis and (b) the minor axis. The inset schematic in each plot shows the initial (black) and final (green) configurations. The minor F-d curve in (b) is superimposed on top of (a) where it is translated to Displacement = 12 mm point.

Therefore, we can deduce that we can tune the nonlinearity of the HECs from strain-softening to hardening by varying compression.

3.8 Conclusion

In summary, we observed the dispersive rarefaction shock (DRS) dynamics in the soft chain of 3D-printed hollow elliptical cylinders (HECs). We experimentally and numerically validated the two principal features of the DRS: the back-tilted wavefront in the form of a rarefaction and the oscillatory wave tail in the form of a dispersive shock. Moreover, we demonstrated that the HEC system supports a slower propagation of DRS given a higher striker impact condition, as a result of the strain-softening nature of this nonlinear dynamical lattice. The proposed HEC system can be potentially applied to the impact mitigation system design in various scientific and engineering applications. Further research can be pursued by modifying the discrete element model (DEM) by adding more degrees of freedom to capture the higher modes of wave propagation. Indeed, as discussed in Section 3.6, while the

phenomenology presented here hinges on the lowest band of its dynamics, the HEC lattice bears intriguing characteristics associated with multiple bands and gaps that are certainly worthwhile of additional exploration. Future studies also include investigating the role of defects (e.g., breather formation) in strain-softening systems. The systematic development of the HEC as a prototypical strain-softening element may also pave the way for exploring heterogeneous chains involving the alternation of softening and hardening nonlinearities, which may manifest unprecedented nonlinear phenomena.

Chapter 4

LINEAR WAVE PROPAGATION IN 1D GRADED HEC

We study the Bloch oscillation of elastic waves in a chain composed of hollow elliptical cylinders (HECs). These HECs are 3D-printed in different wall thicknesses and are arranged to form a graded chain. We find that the frequency band structure of this lattice can be manipulated in a way to create a narrow strip of transmission range sandwiched between slanted stop bands. This enables the trapping of elastic waves at a specific location of the chain, which depends on the input frequency of the propagating elastic waves. This elastic Bloch oscillation in a tailorable 3D-printed system enables the control of energy localization in solids, potentially leading to engineering applications for vibration filtering, energy harvesting, and structural health monitoring.

The rest of the chapter is arranged in the following order. We first explain experimental methods and simulation details in Section 4.1. Then in Section 4.2, we discuss the frequency bands of the graded HEC chain and how it affects the frequency response of the chain. Next, we show the dynamic response of the graded HEC chain to various excitation frequencies and demonstrate the Bloch oscillation in the chain. We discuss tunability of the 3D-printed graded HEC chain and asymmetric linear dynamics in Section 4.3 and 4.4. We finish the chapter with conclusions in Section 4.5.

4.1 Methods

We 3D-print HECs with polylactic acid (PLA) material (Black, Ultimaker). The wall thickness of HECs varies linearly from 0.4 mm to 3 mm in 26 steps. Then we assemble these 26 HECs into a chain, as shown in Fig. 4.1. HECs are aligned through two stainless steel shafts

---

The texts and figures in this chapter have been partly taken from the author's publication [3].

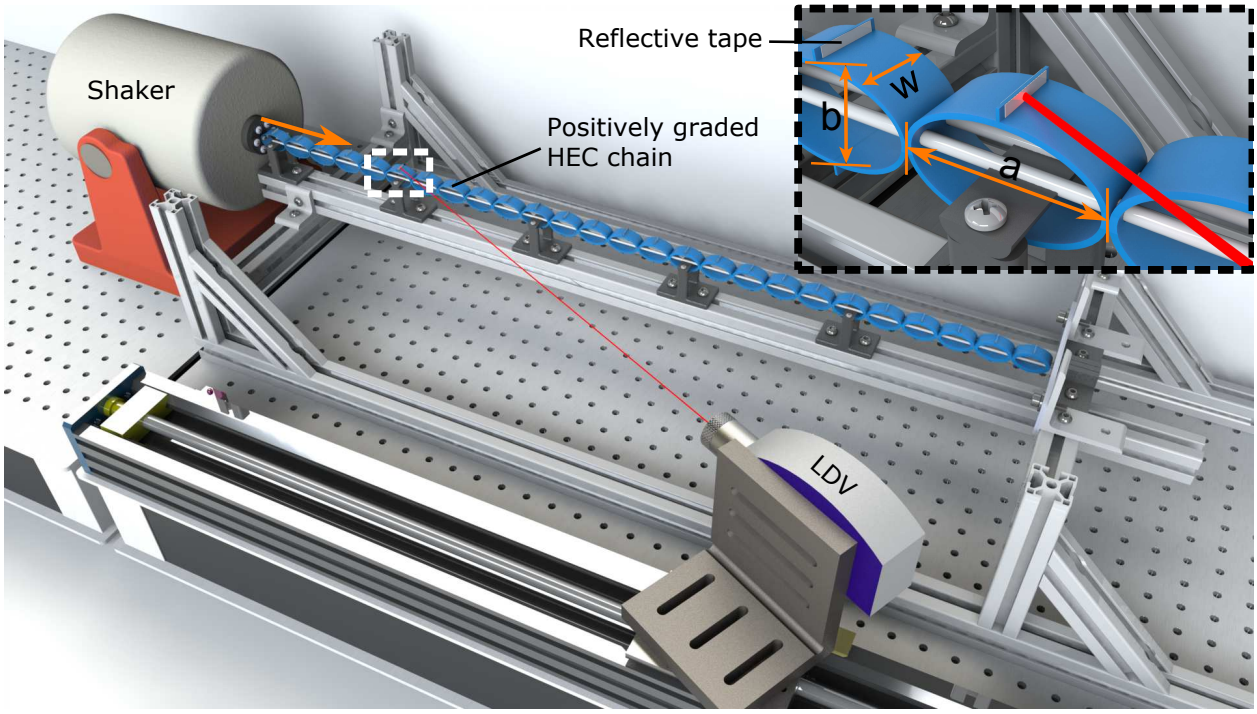

Figure 4.1: A schematic diagram of the experimental setup for the linear perturbation system. One end of the HEC chain is mounted to the shaker head to excite the system longitudinally (orange arrow). The graded HEC chain is securely positioned in the frame through 3D printed jigs. We measure the velocity of each HEC by focusing the laser beam on the reflective tape (the inset on the top right corner, a zoomed-in view of the dashed box in the main image). The dimensions of the HEC are $a = 30$ mm, $b = 18$ mm, and $w = 12$ mm as shown in the inset.

to confine their movement to sliding in the major axis. At the contact point, the HECs are bonded using super glue (Loctite 431) to secure their contact. The first HEC is tightly bolted into the shaker head where the input signal is applied. We apply a precompression of 10 mm to the entire chain and excite the chain at a low amplitude to ensure that the elastic wave is in the linear regime.

We send a frequency sweep signal or a Gaussian pulse to the shaker through a function generator (33220A, Agilent). When the chain is excited, the laser Doppler vibrometer (LDV; Polytec OFV-534) measures the velocity of a single HEC (inset of Fig. 4.1). The velocity data

is acquired by the oscilloscope (DSO-X 3024A, Agilent) and downloaded to a local computer for post-processing. We repeat the experiment five times for statistical treatments.

We use commercial finite element analysis (FEA) software (ABAQUS) to perform numerical analysis. We select the 2D quadratic Timoshenko beam (B22 element) to model the HECs. We simulate only the upper half of the HECs, assuming symmetry about the axial direction. We apply the Neo-Hookean model for implementing the hyperelastic property of the PLA material. We find the material constant of the Neo-Hookean model by fitting to the experimental data ($\mu = 800 \times 10^6$ N/m^2). We ignore the material damping in the simulations.

4.2 Results and Discussion

We first investigate the band structure of the graded HEC chain. By assuming that the unit cell analysis can approximately estimate the *local* frequency band, we assemble the band edge frequencies to build the band structure of the graded chain. Figure 4.2 shows how the band structure of the graded HEC chain is constructed. The first HEC exhibits multiple narrow pass and stop bands (Fig. 4.2(a)). This is because the thin 3D-printed cylinder has multiple eigen frequencies and corresponding eigen modes within the frequency range of interest. The frequency bands move to a higher range as the thickness of the HEC increases due to increase of the bending stiffness associated with the eigen frequencies. The last HEC only has a single pass/stop band within the frequency range of interest. It is notable that the pass/stop band of the last HEC in Fig. 4.2(b) corresponds to the the red dashed box in Fig. 4.2(a). In essence, the dispersion relation of the HECs in the graded chain is nearly a scale-up of that of the first HEC. We only linearly increase the thickness of the HECs and keep everything else the same. Therefore, it is fair for us to expect approximately proportional increase in the natural frequencies. As a result, if we calculate the dispersion relations of all of the individual HECs and assemble them in order, it creates slanted lines of pass bands and stop bands, as shown in Fig. 4.2(c). This resembles the tilted energy band for the electron cases.

Given the interesting slanted band structure, we are curious about the response of the

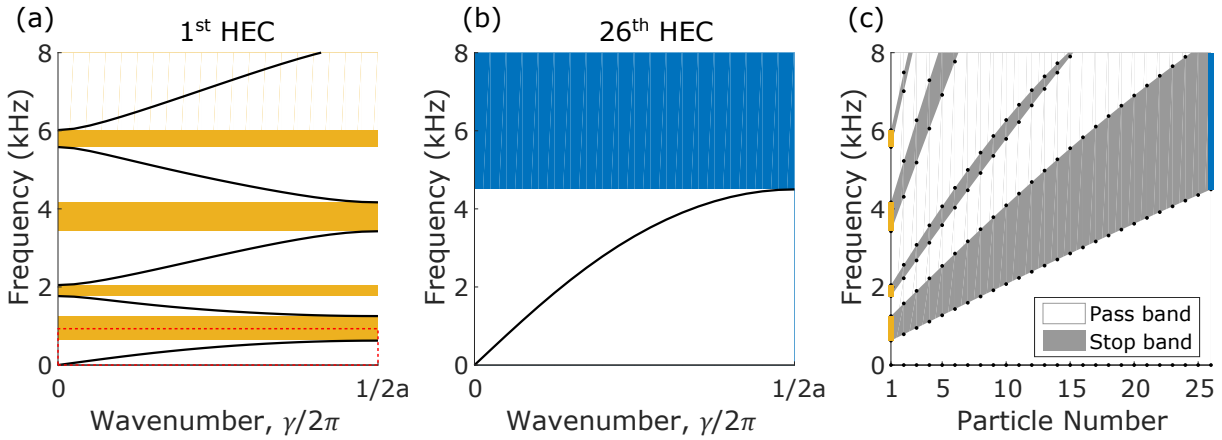

Figure 4.2: Dispersion curves for (a) the fist HEC (thickness of 0.4 mm) and (b) the last HEC (thickness of 3 mm) in the graded chain obtained using FEA. The shaded areas represent stop bands where wave does not propagate, whereas the white area is the pass band where wave transmits. The red box in (a) shows similarity with (b). (c) Band structure of the graded HEC chain. The gray areas indicate the stop band. The yellow and the blue bars come from (a) and (b).

graded HEC chain to single-frequency excitations. To find that, we examine the frequency response of the chain by conducting FEA. We perform steady-state dynamic analysis and calculate the transmission. Figure 4.3(a) shows the transmission level in dB from the FEA result. We observe a transmission band with a positive slope develops from around the origin. We verify the FEA result by conducting experiment. We apply a chirp signal ranging linearly from 0.3 kHz to 8 kHz to the left boundary of the chain and measure the velocity for each HEC. We then perform fast Fourier transform (FFT) on the output data to analyze the frequency components. We observe similar behavior in the experimental result compared to the FEA result, as shown in Fig. 4.3(b). While the highlighted branch continues growing up in the high frequency range, its intensity diminishes. It could be mainly due to the positive gradient of the HEC thickness in the chain. The particle velocity has to decrease as the HEC mass increases to meet the conservation of momentum. Another reason could be the large damping in the high frequency domain.

Let us relate the frequency response (Fig. 4.3(b)) to the band structure (Fig. 4.2(c)).

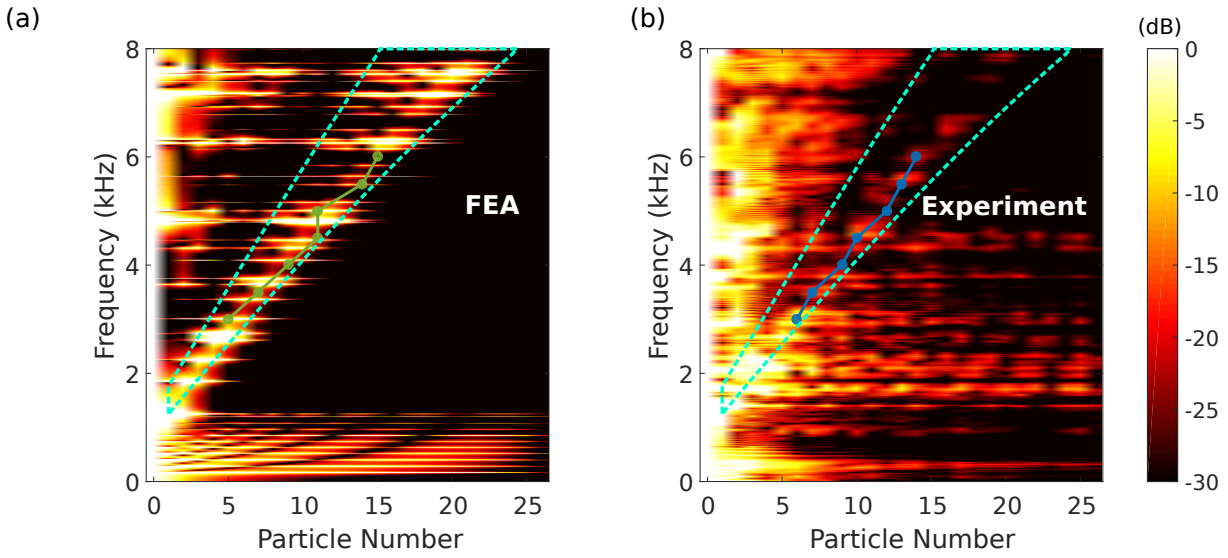

Figure 4.3: Transmission of the velocity signal (a) from the steady-state response using FEA simulation and (b) under the chirp input from the experiment. Brighter color means higher intensity of the signal. The the FEA and the experimental data from Fig. 4.4(d) are superimposed on top of (a) and (b), respectively. The second lowest pass band in Fig. 4.2(c) is superimposed on (a) and (b) in the dashed cyan box.

We observe a near total transmission for the low frequency range (Fig. 4.3(b)) due to the complete pass band throughout the chain (Fig. 4.2(c)). The second pass band is positively sloped and sandwiched between the stop bands with the lower stop band being very thick. The wave can pass through the initial narrow stop bands because the evanescent wave width is possibly wider than the band width. Once the wave reaches the thick stop band, it cannot propagate further. This is what results in the narrow and sloped transmission band in the frequency response (the dashed cyan boxes in Fig 4.3). What this interesting frequency response means is that we have frequency-dependent localization in the graded HEC chain. The narrow transmission band sprouting positively in the frequency-space map causes the wave captured in farther locations at higher frequencies.

To verify that, we analyze transient response of the graded HEC chain. We apply a Gaussian pulse with a central frequency of 5 kHz to the left end and measure the response

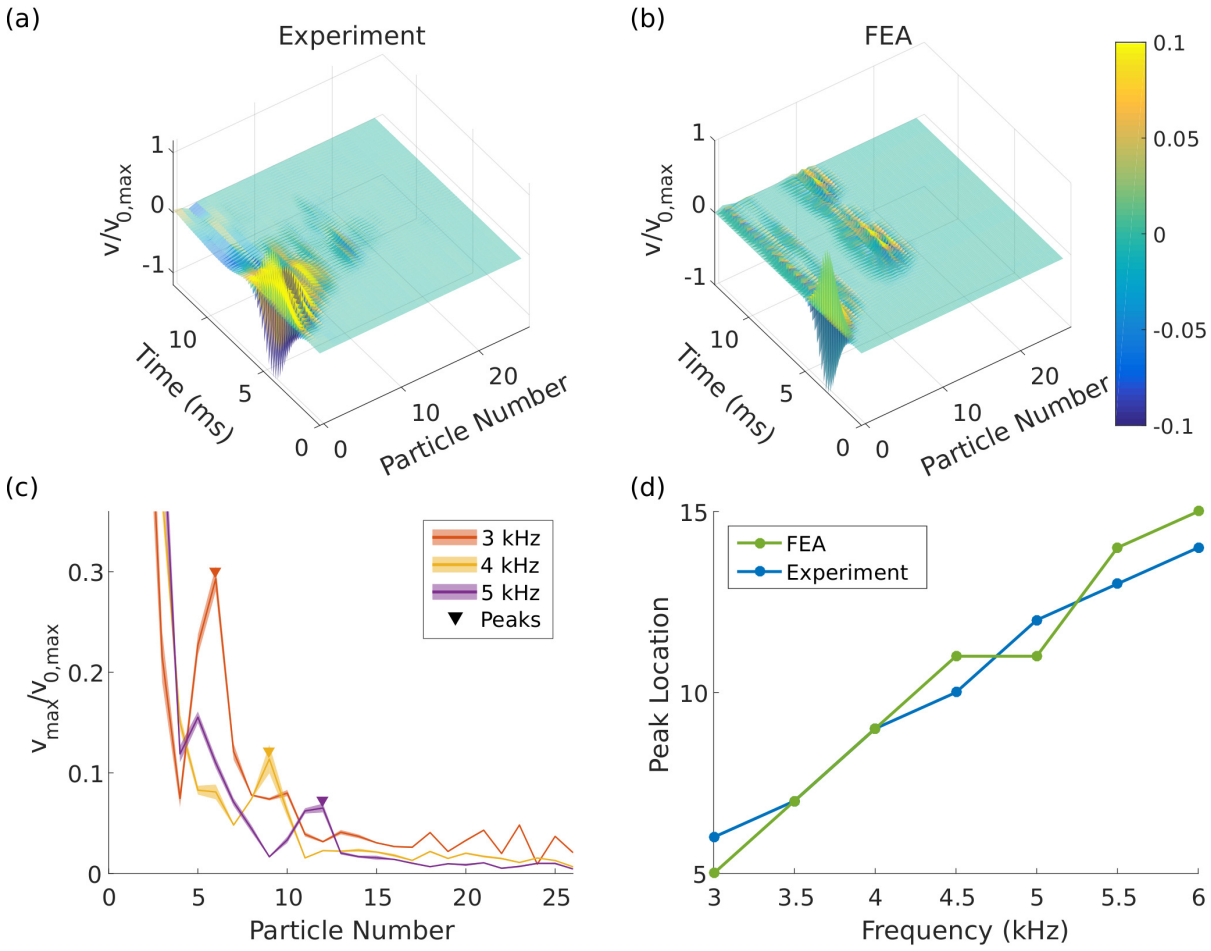

Figure 4.4: Velocity response to the input frequency of 5 kHz mapped in time and space domain, from (a) the experiment and (b) the FEA simulation. The velocity is normalized by the maximum input velocity ($v_{0,max}$). (c) The maximum velocity at each particle number is plotted at 3, 4, and 5 kHz input frequencies in orange, yellow, and purple solid line, respectively. The local peaks are marked with inverted triangles of respective color. The shaded areas represent standard deviations from the experiment. (d) Localization at input frequencies from 3 kHz to 6 kHz with step size of 0.5 kHz, from the experiment (blue line) and the FEA (green line).

of each HEC. The result is plotted in Fig. 4.4(a). The input signal quickly disappears but reappears around the 12th HEC. This signal is trapped and oscillates in this location for around 2 ms and starts to die out. This is a very narrow Bloch oscillation. We observe similar behavior from the FEA in Fig. 4.4(b). The localization of the wave in the middle of the chain keeps its height for a longer time in the simulation. Had we not had friction in the experiment, we would ideally achieve this clear trapping. Overall, we confirm qualitative agreement of the localization effect in the graded HEC chain between the experiment and the FEA.

Next, we investigate the effect of the input frequency on the localization behavior. To achieve that, we conduct the same procedure at different input frequencies and plot the maximum velocity profile, as shown in Fig. 4.4(c). It is evident that the localization peak is positioned farther at higher frequency. The peak amplitude decreases as the input frequency increases. We have pointed out earlier (Fig. 4.3) the reason includes the gradient in mass and the material damping. Figure 4.4(d) shows the localization point with respect to a wide range of input frequencies. Both the experimental data and the FEA result show positive relationship between the input frequencies and the peak locations. They also draw almost linear curves. This aligns very well with the transmission band we found earlier, as shown in the blue and the green curve in Fig. 4.3(a) and (b), respectively. In Section 4.3, we explore the tunability of the HEC system to create nonlinear evolution of band structures.

4.3 Tunability of the 3D printed graded HEC chain

The 3D-printed HEC chains are a highly tunable system, enabling the manipulation of the cell geometry to control their dynamic response. In this section, we explore two possible examples to change the dynamic response of the chain: a) the cell geometry and b) the gradient. The band structure changes depending on the aspect ratio of the unit cell, which ultimately will change the localization position. We can also give a gradient not only in a linear manner but also in nonlinear patterns. This way, we can tune the the frequency-localization relationship from linear to nonlinear.

First, we study the effect of the aspect ratio of the HEC on the dispersion relation of the graded HEC chain. In the previous sections, we only show the result for the aspect ratio of 5:3 which is repeated in Fig. 4.5(a). The aspect ratio is defined as the longitudinal to the transverse direction length. If we decrease the aspect ratio, i.e., change the ellipse to a circle (Fig. 4.5(b)) and to the other side of the ellipse (Fig. 4.5(c)), we see the first thick stop band shrinks and the second thin stop band expands. Consequently, the slanted pass band widens. As a result, we expect to observe clear Bloch oscillations as the wave is localized within a wide length of the chain.

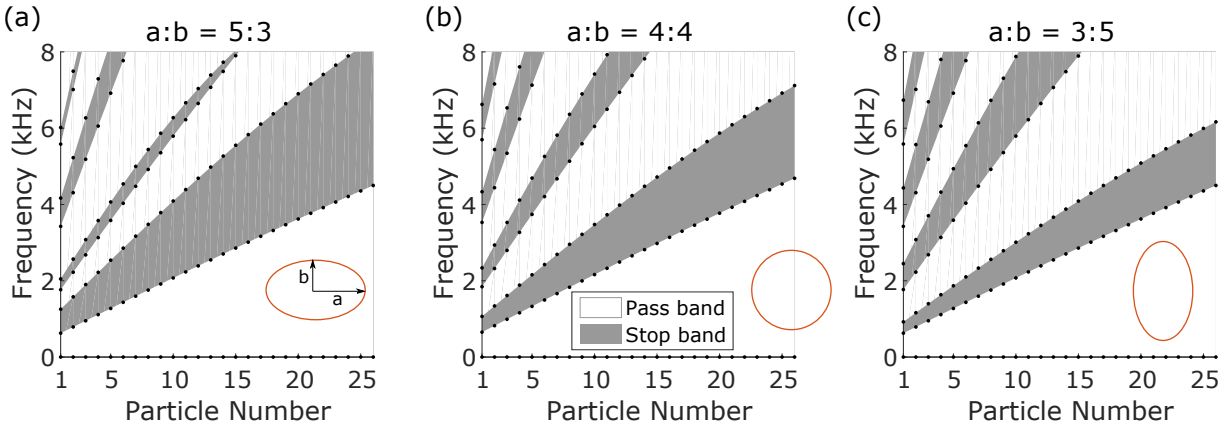

Figure 4.5: The band structure of the graded HEC chain whose aspect ratio, a:b (longitudinal to transverse), is (a) 5:3, (b) 4:4, and (c) 3:5. The insets are the HEC configurations.

Next, we investigate the effect of the gradient on the dynamics of the graded HEC chain. We vary the thickness exponentially from 0.4 mm to 3 mm and calculate the dispersion relation for each HEC. Then we construct the band structure by assembling the individual dispersion relations, as shown in Fig. 4.6(a). It is evident that the pass and the stop bands are curved rather than straight (Fig. 4.3(c)) in spatial domain. As a result, we observe a curved transmission branch in the frequency response in Fig. 4.6(b). This shows the capability of the graded HEC system to change the localization point by tuning the gradient parameters.

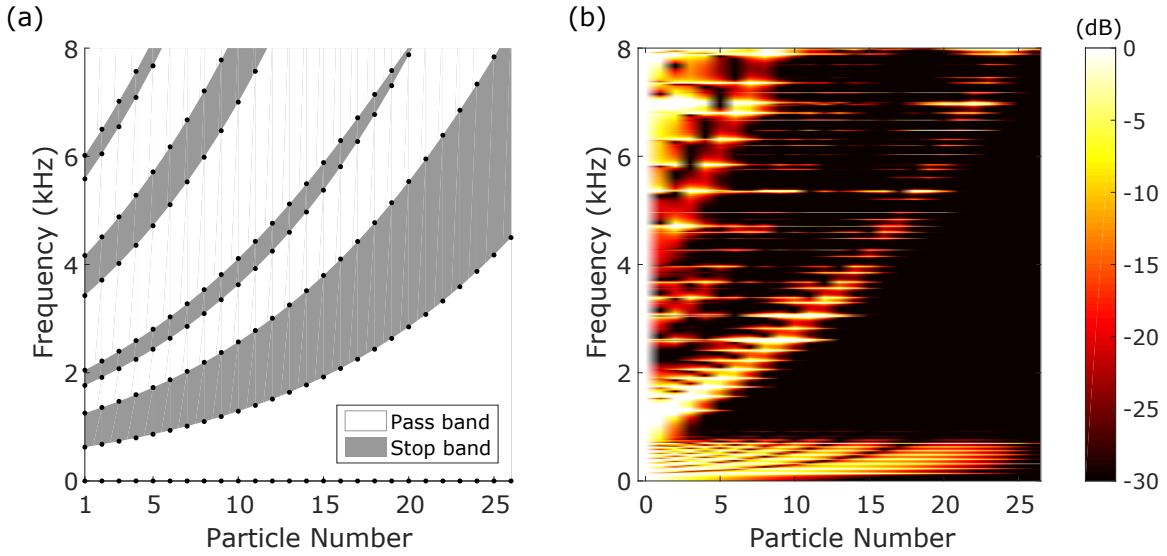

Figure 4.6: (a) Band structure of the HEC chain with exponential thickness gradient. Wave can only travel in the pass band. (b) Frequency response of the same chain using steady-state analysis.

4.4 Negative thickness gradient

In previous sections, we only discuss the HEC chain with positive thickness gradient. We can easily investigate linear dynamics of the negative gradient HEC chain by simply flipping the chain in the opposite direction. In this section, we discuss how the dynamics changes in the negative thickness gradient. We measure the frequency response of the chain and compare it with the FEA result and the band structure. We follow the exact same procedure as Section 4.1 and 4.2. We apply a chirp signal ranging between 0.3 kHz and 8 kHz to the thickest HEC and measure the velocity of each HEC. We see a high transmission area (the bright color) with a negative slope, as shown in Fig. 4.7(a). Unlike the positive gradient HEC chain (Fig. 4.3(a)), the transmission level is kept high to the end of the chain. The HEC mass decreases towards the chain end, resulting in higher particle velocity to meet the conservation of momentum. This agrees well with the FEA result in Fig. 4.7(b). The high transmission in Fig. 4.7(a) and (b) corresponds to the first pass band in the band structure in

Fig. 4.7(c). This band structure is a mere flip in the horizontal direction of Fig. 4.2(c). Due to the thick stop band from the thick HECs, wave cannot propagate through the chain at high frequency range (4.5 kHz - 8 kHz). For the same reason, the wave in the low frequency range stops traveling once they hit this boundary. In other words, the wave is reflected against the first stop band and thus, is not transmitted through the chain.

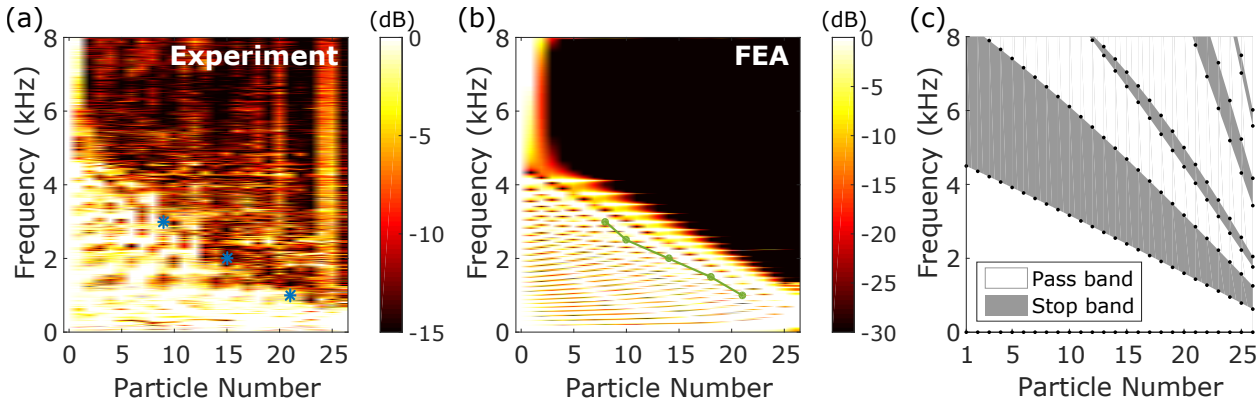

Figure 4.7: Transmission of the velocity signal of the HEC chain with negative gradient (a) under the chirp input from the experiment and (b) from the steady-state response using FEA simulation. The blue markers and the green line are superimposed from Fig. 4.8(d). (c) Band structure of the negatively-graded HEC chain. The gray area indicate the stop band where wave does not propagate, whereas the white area is the pass band where wave transmits.

We verify the reflection effect of the negatively-graded HEC chain at different frequencies. We excite the chain with a Gaussian pulse at 2 kHz and measure the velocity response. As seen in Fig. 4.8(a), the input wave quickly dies and reflects back at around 21st HEC. We observe a very similar behavior in FEA result in Fig. 4.8(b). This is so-called boomerang or rainbow effect, which has been reported in [52, 89]. The quantitative difference of amplitude between the experimental and computational results is due to the friction and damping effects.

We measure the transient response at other input frequencies and plot the maximum velocity at each HEC in Fig. 4.8(c). We notice that the reflection location comes close to the

excitation point at the higher input frequency. In other words, the wave is reflected earlier at the higher excitation frequency. We also find that the maximum velocity amplitude increases towards the chain end. As mentioned in the previous paragraph, the decreasing mass plays a role to this amplified response. We confirm again that the experiment (solid lines) and the FEA (dashed lines) are in good agreement. We plot the reflection point with respect to the input frequency in Fig. 4.8(d). We can clearly see the negative relationship between the reflection location and the input frequency. Moreover, the filtering locations match the transmission boarder as indicated by the star and circular marks in Fig. 4.7(a) and (b), respectively.

4.5 Conclusion

In summary, we investigated the elastic Wannier-Stark ladders and the Bloch oscillations in a 3D-printed, graded HEC chain. We experimentally and numerically demonstrated that the location of the Bloch oscillation depends on the input frequency in our system. Within the frequency range of interest, we find that the higher the input frequency is, the farther the localization happens. This is due to the slanted band structure, or the Wannier-Stark ladders, of the graded HEC chain.

This study showcases that the design boundary for the band structure (i.e., bandgap) engineering can be broadened by the soft lattices made of 3D-printed architectures. This can enable an enhanced degree of freedom in controlling stress waves in solids, thereby realizing a plethora of novel wave dynamics. While this study focused on the Bloch oscillations in the graded lattice, the same system in the opposite gradient can provide another interesting phenomenon, so-called the rainbow (or boomerang) effect (Section 4.4).

The findings from this study can be integrated into various engineering applications, such as energy harvestor, structural health monitoring, and nondestructive evaluation systems, which require energy trapping. We also see the possibility of shedding light on the design of artificial cochlea, as it captures the wave of different frequency at different locations.

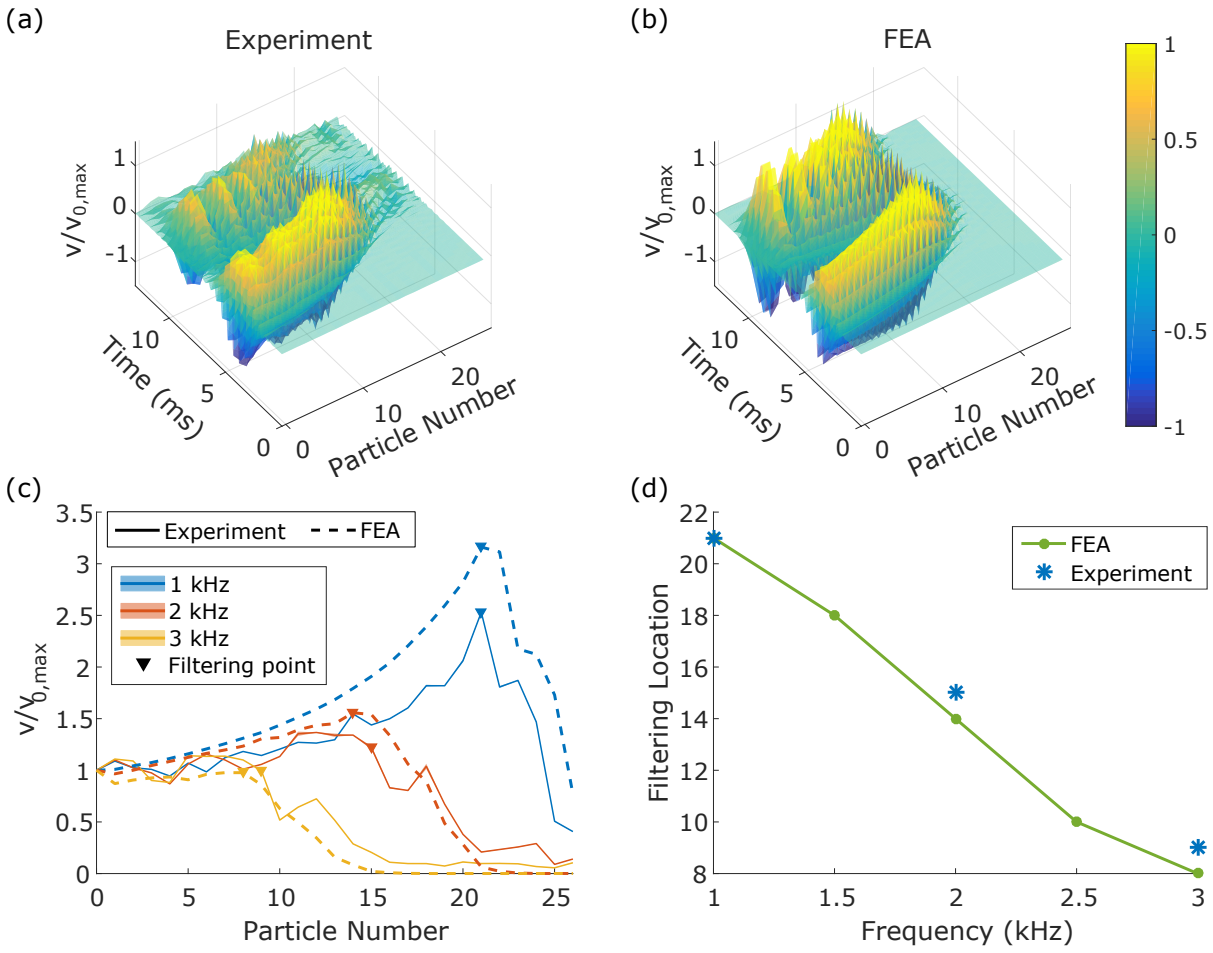

Figure 4.8: Velocity response at the input frequency of 2 kHz mapped in time and space domain, from (a) the experiment and (b) the FEA simulation of the negatively-graded HEC chain. The velocity is normalized by the maximum input velocity ($v_{0,max}$). (c) The maximum normalized velocity of the propagating wave (excluding reflected wave) at each HEC. The blue, orange, and yellow solid lines indicate the input frequency of 1, 2, and 3 kHz, respectively. The solid lines represent experimental result and the dashed lines represent FEA result. The shaded area, although hardly visible, represent the standard deviation from the experiment. We find the point where the wave amplitude starts to decline and mark with inverted triangles. These locations are plotted with respect to the corresponding input frequency in (d). The experimental results are plotted as asterisk markers and the FEA results are plotted in the green solid lines with circular markers.

Chapter 5

NONLINEAR WAVE PROPAGATION IN 1D AND 2D GRADED HEC

In this chapter, we propose a 3D-printed graded lattice made of hollow elliptical cylinders (HECs) as a new way to design impact mitigation systems. We observe asymmetric dynamics in the graded HEC chains with increasing and decreasing stiffness. Specifically, the increasing stiffness chain shows an acceleration of the propagating waves, while the decreasing stiffness chain shows the opposite. From the standpoint of impact mitigation, the decreasing stiffness chain combined with the strain-softening behavior of HECs results in an order-of-magnitude improvement in force attenuation compared to the increasing stiffness chain. We extend this finding to the graded 2D arrays and demonstrate a similar trend of wave transmission efficiency contrast between the increasing and decreasing stiffness lattices. The 3D-printed HEC lattices shown in this study can lead to the development of a new type of impact mitigating and shock absorbing structures.

The rest of the chapter is arranged in the following manner. In Section 5.1, we provide details on the technical approach. Section 5.2.1 describes the asymmetric nonlinear dynamics in the HEC chain with a positive and a negative gradient direction. We experimentally demonstrate the simulated dynamics in the graded HEC chains. In Section 5.2.2, we conduct rigorous comparison of the impact mitigation performance between the two opposite gradient chains. Section 5.2.3 suggests a potential extension of the 1D graded HEC chains to the 2D graded HEC array. We describe additional analysis in Section 5.3-5.5. We finish this chapter with conclusion in Section 5.6.

The texts and figures in this chapter have been partly taken from the author's publication [2].

5.1 Methods

We first perform 1D experiment as follows: we 3D-print 26 HECs using PLA material with their wall thicknesses linearly varying from 0.4 mm to 3 mm. See Section 3.5 for the detailed geometry and force-displacement relationship of the HECs under the variation of their wall thicknesses. We align these HECs into two different chain configurations: (i) a chain with the increasing HEC thicknesses (called a thickening chain for the rest of this article) and (ii) a chain with the decreasing HEC thicknesses (i.e., thinning chain). Figure 5.1(a) shows an experimental setup of the thinning chain. Here, the HECs are printed with two small holes (diameter of 2.50 mm) along the major axis, such that they are allowed to slide along the horizontal direction by using a pair of stainless steel rods (diameter of 2.38 mm) that penetrate through all HECs (inset of Fig. 5.1(a)). These rods are held by 3D-printed supports to prevent them from bending. To ensure their mechanical contact, the HECs are bonded together using glue (Loctite 431).

For the application of mechanical impact, we send an impulse signal to a shaker (LDS V406, B&K) such that it launches a rectangular striker mass towards the one end of the HEC chain at a desired velocity. The other end of the chain is bounded by a piezoelectric sensor (208C02, PCB Piezotronics), which is mounted on the rigid chassis and is used to measure the transmitted forces through the HEC chain. The striker mass (m_s = 4.3 g) is 10 times larger than the mass (m) of the thinnest cylinder. When the striker hits the chain, it triggers the high speed camera (Phantom v1211) to start recording. The high speed camera moves along the linear stage, capturing three cylinders at a time at 40000 fps. The measurements are made at every other cylinder location, and we iterate the experiment five times for statistical treatments. To facilitate the tracking of the HECs' translational motions, we print bosses on the top and bottom of each HEC (see the inset of Fig. 5.1(a) or Fig. 3.5(a) in Section 3.5). We use the digital image correlation technique to measure the displacements of HECs [1]. The data collected are stitched together, and the aligned data after reconstruction in the space domain are presented in the results hereafter.

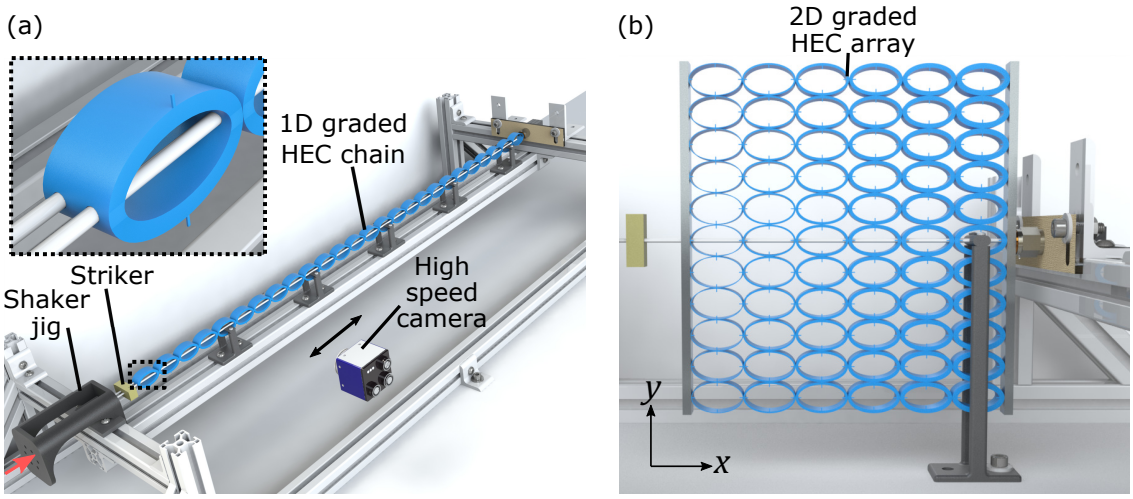

Figure 5.1: (a) A schematic diagram of the 1D HEC setup for dynamic testing. Shaker jig is attached to the shaker head (not shown but indicated by the red arrow) to slide the striker. The graded HEC chain is impacted by the striker on the left end at the input velocity, $v_s = 2.95 \pm 0.09$ m/s. The right end is in contact with a piezoelectric sensor. The inset is a close-up view of the single HEC inside the dotted box. (b) A schematic diagram of experiment setup for the 2D graded HEC array.

To compare with the experimental results, we perform numerical analysis using commercial finite element analysis (FEA) software (ABAQUS). We apply the Timoshenko beam model (B22 element) to capture the behavior of the HECs. To take into account the hyperelastic behavior of PLA, we implement the Neo-Hookean model. We find its shear modulus and material damping factor by fitting the experimental data based on uniaxial compression tests.

We also compose a 2D graded HEC array as shown in Fig. 5.1(b). We print 11 rows of HECs whose thicknesses vary linearly from 0.4 mm to 3 mm along the horizontal direction. Then we carefully align them and glue between the rows into a 6×11 array. Similar to the 1D setup, the HECs in the middle row are guided by a pair of stainless steel shafts. We cut two 5-mm-thick aluminum plates to a size of 200 mm by 12 mm with two small holes (diameter of 2.5 mm) and glue them to the left and the right end of the graded HEC array. These plates and HEC arrays are equivalent to the facesheet and core of sandwich structures, respectively,

in 2D representation. The right plate is in contact with the piezoelectric sensor to record the transmitted forces through this 2D HEC array. To prevent any rotational dynamics of the array, we firmly hold the horizontal guiding rods by using a 3D-printed support. The way we apply striker input is the same as that in the 1D chain experiment.

5.2 Results and Discussion

5.2.1 Asymmetric impact response

Figure 5.2 shows experimental (top row) and numerical (middle) results of HECs' velocity profiles for thinning (left) and thickening (right) chains. It is notable that the thinning and the thickening chain show completely different dynamic behaviors. The first feature to notice is the acceleration/deceleration of the propagating waves depending on the gradient direction. This phenomenon is closely related to the mass and stiffness of the unit cells composing the chain. In case of the thinning chain, the contact stiffness decreases towards the end of the chain. Lower stiffness results in the decrease in wave speed (Fig. 5.2(a) and (c)). Furthermore, the negative mass gradient will amplify the propagating wave amplitude, slowing down the wave due to the effective strain-softening nature of the HECs. In the same manner, acceleration occurs in the opposite direction (Fig. 5.2(b) and (d)). The experimental data (Fig. 5.2(a) and (b)) corroborate the FEA results (Fig. 5.2(c) and (d)) for both thinning and thickening chains.

The accelerating and decelerating waves in graded chains have been also explored in previous studies [55,58,59,62,64,90]. However, our system is different from those in previous studies in that (1) the unit cells are bonded together supporting both compressive and tensile motions, and (2) they are deformed modestly in a weakly nonlinear regime. As a result, we observe unique wave dynamics in the HEC system, such as the formation of weakly nonlinear pulses followed by oscillatory tails due to tensile motions (see the ripples in Fig. 5.2).

Another feature to notice is the amplitude change. The amplitude significantly decreases as the wave approaches the end of the thickening chain (Fig. 5.2(b) and (d)). However,

in the thinning case, the amplitude increases minutely as the wave propagates along the chain (Fig. 5.2(a) and (c)). This amplitude change is obvious if we look at the individual wave profiles in Fig. 5.2(e) and (f). This attenuation/amplification of the propagating wave can be also explained by the change in mass and stiffness within the graded chain. In the thickening chain, the mass of the HEC increases, thereby decreasing the particle velocity to satisfy the conservation of momentum principle. Moreover, the increasing stiffness results in a faster group velocity, which extends the width of the leading wave and contributes to the attenuation of the wave amplitude. On the contrary, in the thinning chain, the HEC masses become lighter towards the end, resulting in higher particle velocities. Contact stiffness also decreases in this case, which contributes to narrowing width and thus amplifying the wave. More details on the effect of the contact stiffness and the mass are described in Section 5.3. The amplitude change also is affected by the energy transfer from kinetic energy to strain energy. See Section 5.4 for the energy analysis.

The asymmetric wave propagation in opposite directions is in reminiscence of the study by [78, 79]. They take advantage of the asymmetry of their system to realize non-reciprocal wave propagation by selectively triggering nonlinear instability in a single direction. The transmission induced by overcoming the threshold with high amplitude input is called supra-transmission. Similarly, for the thinning chain in our system, the striker impact contains a wide range of frequencies (Fig. 5.10(a) in Section 5.5) and the output signal contains most of the input frequency components, despite the significant transfer to the low frequency modes. The thickening chain does not transfer much energy to the end of the chain, as seen in Fig. 5.10(b) in Section 5.5. As a result, we confirm a similar trend of asymmetric supra-transmission in our graded HEC chain, by leveraging not the bistability of unit cells, but their arrangements in gradient. More details on the spectral analysis can be found in Section 5.5.

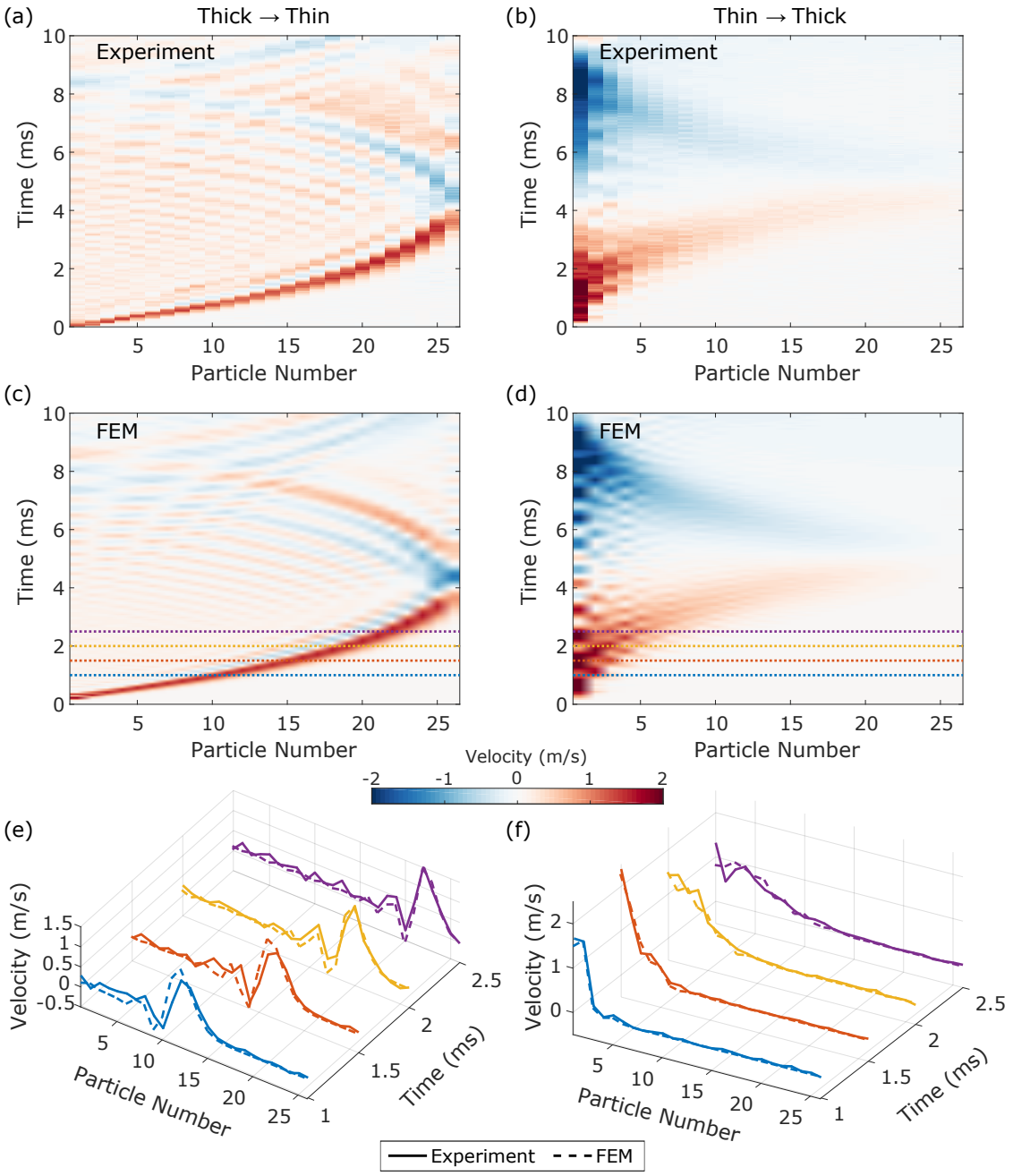

Figure 5.2: Surface map of HECs' velocity profiles in space and time domain for (a) the thinning and (b) the thickening chain, based on the experimental data. The FEA results for the corresponding configurations are shown in (c) and (d). The cross sections along the dotted lines in (c) and (d) are plotted in (e) and (f) in dashed curves, respectively. The solid curves represent the corresponding velocity profiles from the experimental data.

5.2.2 Impact mitigation

We evaluate the shock absorption performance of the graded HEC chains by investigating their transmitted force profiles (Fig. 5.3). In the thinning chain, the initially localized force peak disperses slowly as the wave propagates along the chain (Fig. 5.3(a)). In the thickening chain, the initially dispersed force profile tends to become highly localized towards the end of the chain (Fig. 5.3(b)). This difference is evident if we compare the force profiles measured at the end of the chain by using a force sensor (Fig. 5.3(c)). Here, we also include experimental results for comparison (circular markers). We observe a solitary wave-like localized pulse in the thickening chain (see the dashed red curve based on the FEM result, which show no oscillatory tails). On the other hand, the thinning chain exhibits a small-amplitude leading pulse followed by oscillations. While there exist noticeable discrepancies between the experimental and computational results possibly due to friction and material damping, we still witness the qualitative difference in the empirical force packets between the thinning and thickening chains.

These force profiles may look contradictory to the velocity profiles presented in Section 5.2.1. In the velocity profiles, the thinning chain showed the focusing behavior of wave packets (left column in Fig. 5.2), while the thickening chain exhibited the attenuation of those packets (right column in Fig. 5.2). This seemingly contradictory behavior between velocity and force profiles can be explained by the energy analysis. We calculate the evolution of kinetic and strain energy stored in the HEC system over the span of 5 ms, which covers a travel of the initial impact to the end of the chain (Fig. 5.4). In the thinning chain, we observe the kinetic energy and the strain energy reach an equilibrium point where their levels are comparable (Fig. 5.4(a)). In the thickening chain, however, most kinetic energy is converted into the strain energy. In other words, in the thinning chain, the impulse facilitates the rattling of the HECs after it passes by the chain (thus causing the oscillatory tails as witnessed in Fig. 5.3(c)), while the thickening chain rather piles up its energy into the strain energy instead of shedding it into dynamic energy. This is the key difference in

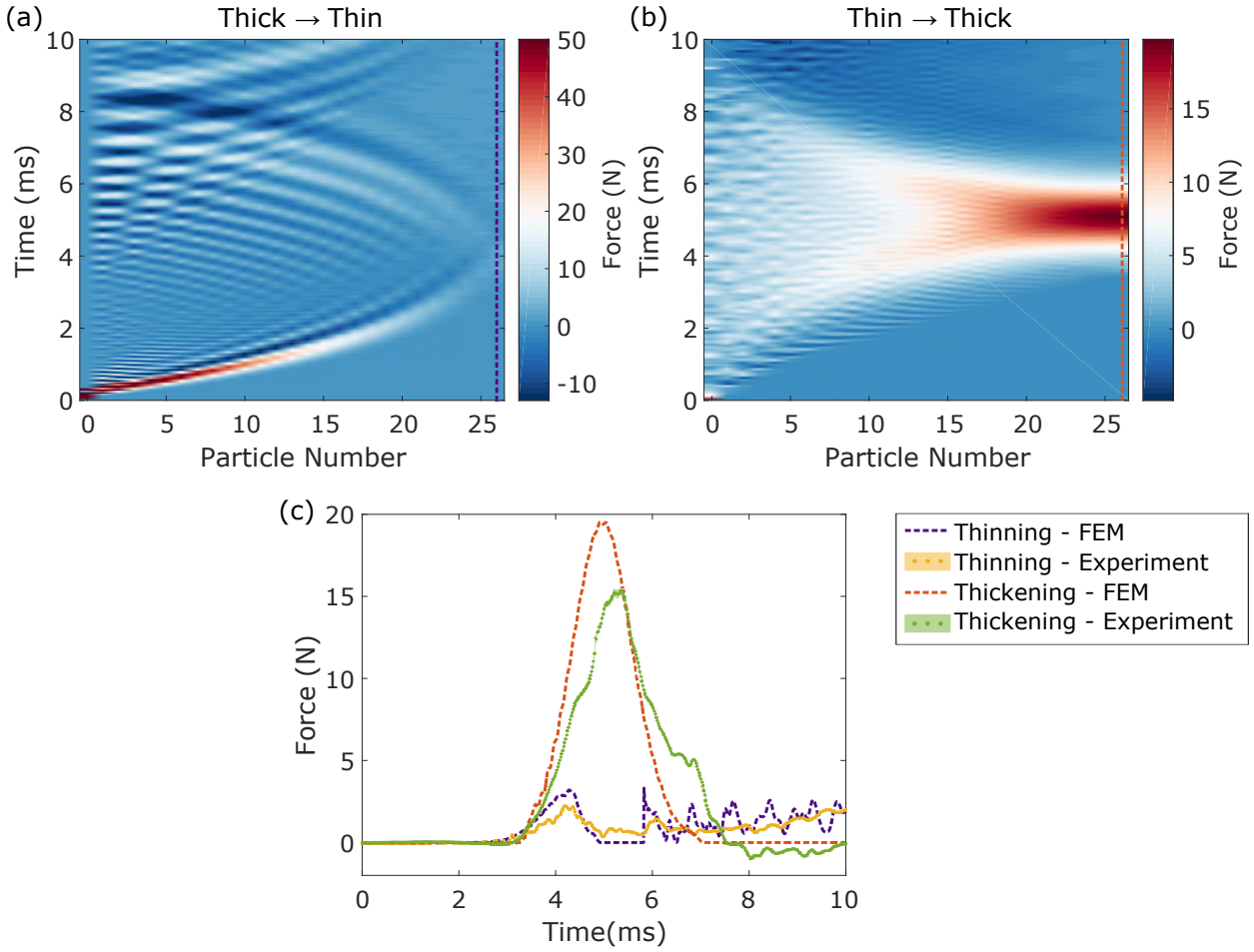

Figure 5.3: Contact force between HECs in (a) the thinning chain and (b) the thickening chain. The contact force is calculated in ABAQUS simulations. 0 index means the striker. Negative force means tensile direction. The dashed lines at $n = 26$ indicate the output force profiles which are plotted in (c). (c) Contact force output at the right boundary. The purple and red dashed curves show the output force in the thinning and the thickening HEC chain from FEA results, respectively. We run 10 experiments and plot the average values in circular markers and the standard deviations in shaded areas (yellow for the thinning and green for the thickening HEC chain). The striker velocity $v_s = 3.00 \pm 0.07$ m/s).

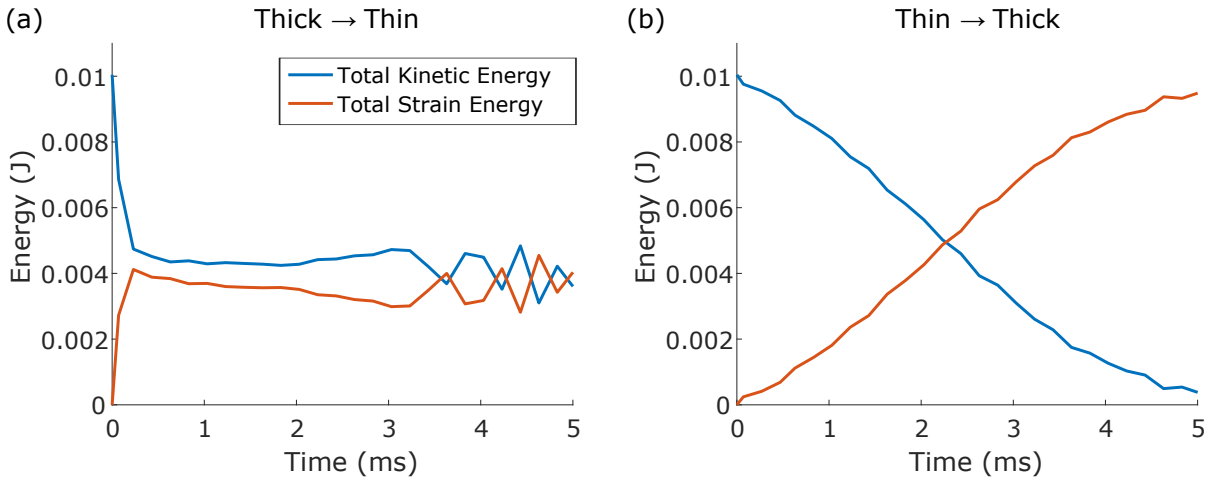

Figure 5.4: Kinetic energy (blue curve) and strain energy (orange curve) of the entire model in (a) the thinning chain and (b) the thickening chain based on numerical simulations without damping.

energy transfer between the thinning and thickening chains. Since the velocity profiles are directly related to the kinetic energy, the trend looked contradictory to the force profiles that are associated with the strain energy. Further details on energy analysis can be found in Section 5.4.

5.2.3 Two-dimensional expansion

Now we assess the feasibility of extending the 1D HEC system into a 2D one, such that it can be potentially used as a core material for impact mitigating structures. To this end, we build a sandwich structure as shown in Fig. 5.1(b). Here, the arrangement is in a pseudo-2D manner, graded in the x direction and homogeneous in the y direction. Given the shallow thickness of the layer (12 mm), we impose the plane stress condition in the out-of-plane direction. We measure the transmitted force profiles at the right end of the prototype and plot them in yellow curves for the thinning (Fig. 5.5(a)) and the thickening (Fig. 5.5(b)) array. The corresponding numerical data are also plotted in red curves in Fig. 5.5. Consistent with the 1D chain result, the maximum force at the wall in the thinning array is lower than that

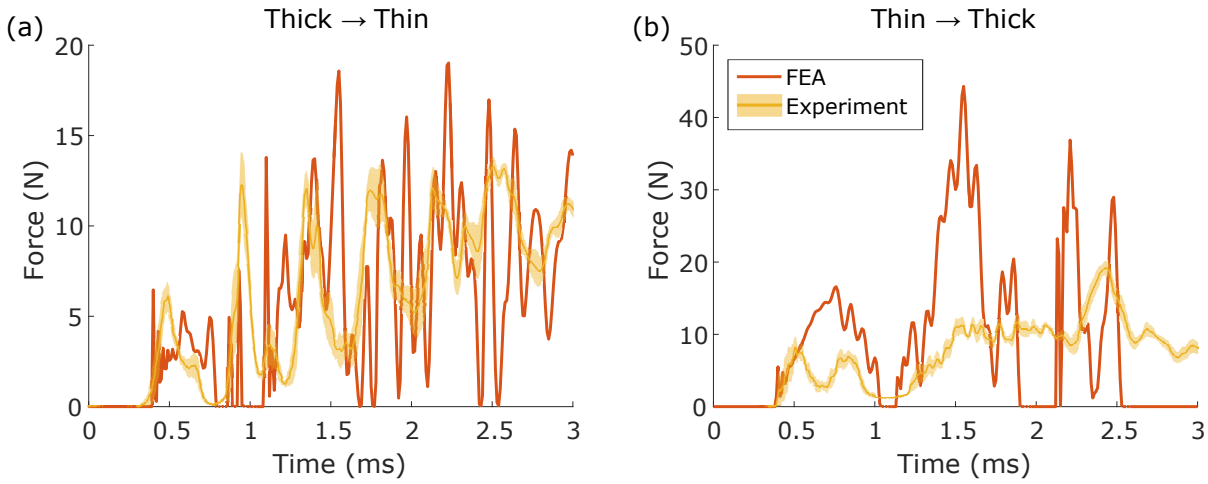

Figure 5.5: Contact forces at the output boundary are plotted for (a) the 2D thinning array and (b) the 2D thickening array. The array size is 6×11. We run 10 experiments and plot the average in the yellow solid line and the standard deviations in the yellow shaded areas ($v_s = 2.93 \pm 0.05$ m/s).

of the thickening chain. However, the performance of the thinning chain is better than the thickening chain only by twice, which is smaller than the 7-fold improvement observed in the 1D system. This is likely due to the transverse dispersion of energy, as well as the short chain length in 2D.

The dispersive effect can be clearly seen in numerical simulations (Fig. 5.6), where the thickening lattice immediately radiates energy in the transverse direction (y-direction) as the striker hits the plate, while the thinning lattice does not. Despite this transverse dispersion effect, we still verify the asymmetric wave propagation in the 2D graded HEC array. Particularly, the amplifying velocity towards the end of the thinning array is consistent with the dynamics we observe in the 1D thinning chain (Fig. 5.2(a)). Likewise, the localization of the velocity at the input boundary of the thickening array is in agreement with the 1D thickening chain (Fig. 5.2(b)).

To investigate the chain size effect, we model a larger array, 120×11, as shown in Fig. 5.7(a) and examine how the impact absorbing level changes. A striker with the mass of

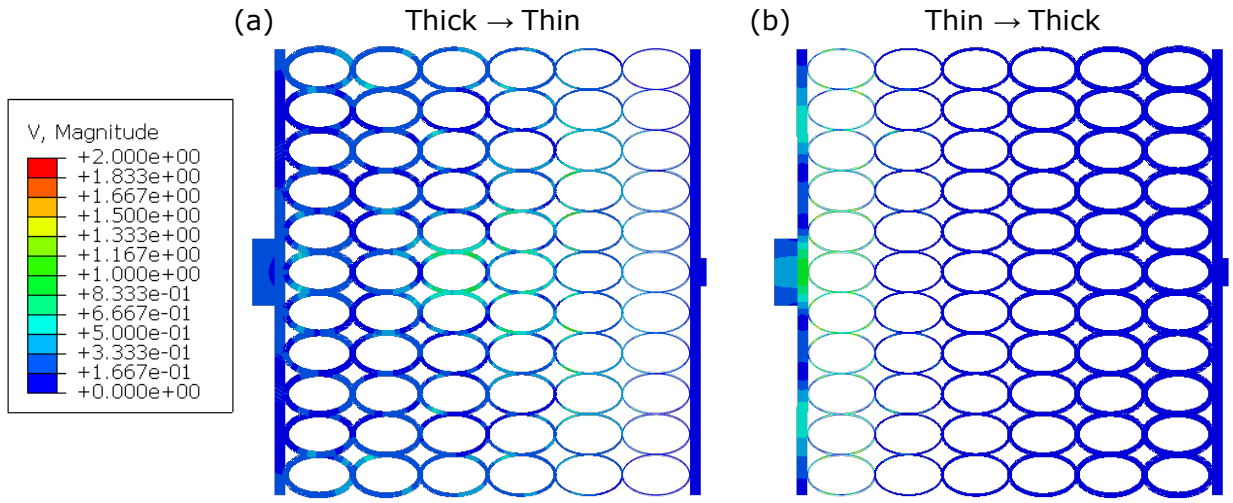

Figure 5.6: Velocity contour of the 2D model from ABAQUS for (a) thinning HEC and (b) thickening HEC array at $t = 0.4$ ms.

30 g is applied at an initial velocity of 3 m/s. We observe an order-of-magnitude difference in the maximum output force between the thinning and the thickening arrays (Fig. 5.7(b)). The oscillating envelope of the force profile is due to the vibrations of the HECs. In fact, the dominant frequency component of the wave profile is 1.2 kHz, which is around the 1^{st} vibration mode of the thickest HECs and the 2^{nd} vibration mode of the thinnest HECs. This numerical result hints that the proposed 2D HEC lattices can be potentially used as a core material in sandwich structures for incurring asymmetric wave propagation and thus efficient impact mitigation.

5.3 Force-displacement relationship of HECs

In this study, we achieve the variations of the HECs' stiffness by modifying their wall thicknesses. To assess this thickness effect, we numerically calculate the force-displacement relationship between adjacent cylinders in the graded HEC chain using FEA (Fig. 5.8(a) for the geometrical configuration of the gradient chain composed of HECs). We see from Fig. 5.8(b) that the HECs show effective strain-softening behavior, i.e., decreasing stiffness (the slope

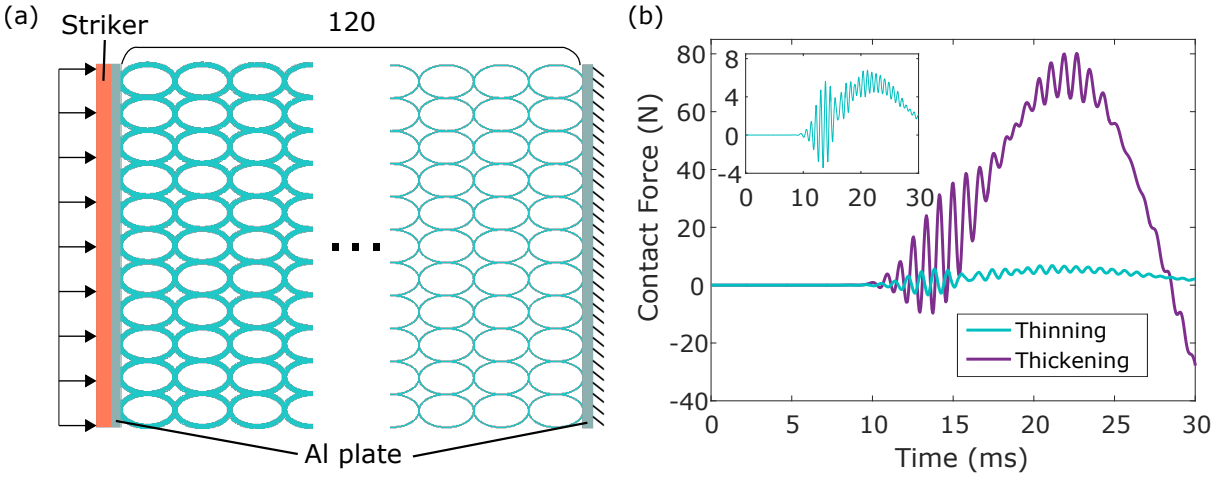

Figure 5.7: (a) The schematic of the 120×11 HEC model. The thickness gradient is assigned such that it varies from 3 mm to 0.4 mm along the impact direction. The 2D HEC core is bonded and sandwiched between aluminum plates. The plate thickness is determined such that its mass is the same as the thickest HEC column's mass. (b) FEA analysis on contact force at the right end for 2D thinning array (turquoise line) and 2D thickening array (purple line). The inset shows the thinning chain response in a magnified view. Damping is not considered in these simulations.

of the force-displacement curve) in compression. This holds true regardless of the thickness of the HECs, as seen from the force-displacement curve of thickest pair (the orange curve in Fig. 5.8(b)) to the thinnest pair of HECs (the yellow curve in the inset of Fig. 5.8(b)). In fact, the force-displacement curve of the HEC nearly scales up as its thickness increases. As a result, the graded HEC chain exhibits a gradual change of force-displacement relationship, leading to a universal power-law relationship [1].

5.4 Energy analysis of graded HEC chain

In this section, we investigate the evolution of kinetic and strain energy during the propagation of waves in thinning and thickening HEC chains. We export kinetic and strain energy data from ABAQUS simulation results and plot the contour map in both time and space domain in Fig. 5.9. For the thinning chain, we see a large portion of the kinetic energy (Fig. 5.9(a)) is transmitted towards the end of the chain, even showing clear reflection from

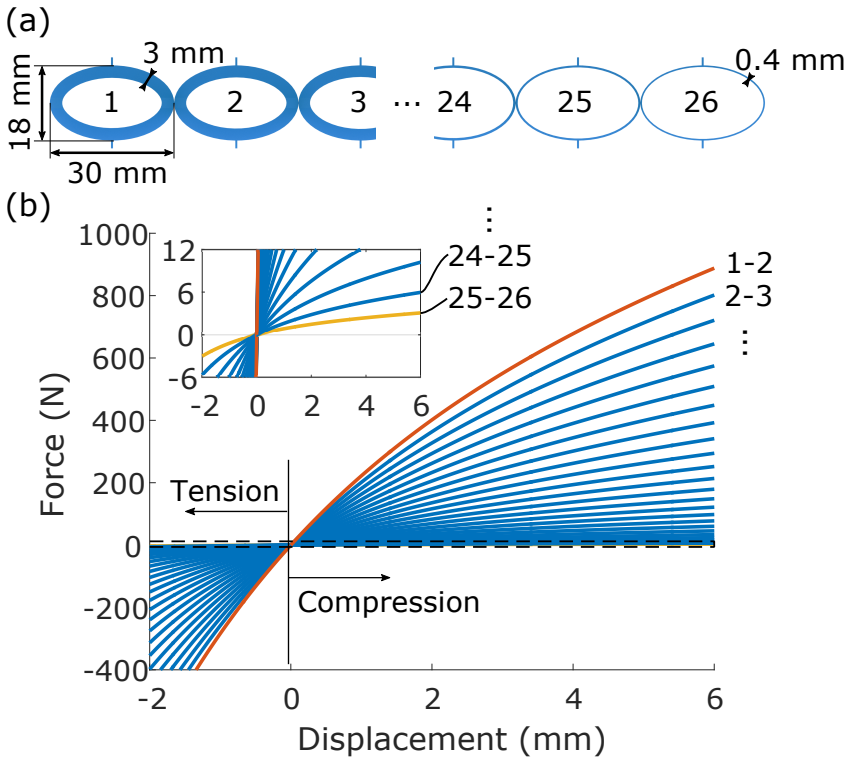

Figure 5.8: (a) An illustration of the graded HEC chain and its dimensions. The chain is composed of $N = 26$ HECs with linearly graded thickness from 3 mm to 0.4 mm. The out-of-plane width is 12 mm. (b) The force-displacement curve between adjacent HECs in the graded chain. The compressive deformation is plotted positive. The force-displacement relationship of cylinder 1 and 2 is plotted in the orange curve. Likewise, the force-displacement relationship between cylinder 2 and 3, 3 and 4, and so on (refer to (a) for cylinder numbers) are plotted respectively from the top to the bottom. The inset shows an enlarged view of the force-displacement curves for the last few cylinder pairs.

the boundary. An equivalent amount of the strain energy (Fig. 5.9(c)) is also observed, but it diminishes noticeably as the wave propagates through the chain. The thickening chain shows a different trend of kinetic and strain energy transmission. We see a drastic reduction of the kinetic energy in the first few HECs in the chain (Fig. 5.9(b)). This kinetic energy lost is transferred to the strain energy as shown by the highlighted area in Fig. 5.9(d). This energy transfer phenomenon is again due to the large deformation of the thin HECs in the early part of the chain, caused by the striker impact. This corroborates the results reported in the velocity and force profiles as shown in Fig. 5.2 and 5.3.

5.5 Spectrum interpretation of graded HEC chain

We perform Fast Fourier Transform (FFT) on the velocity data to investigate the frequency components in the propagating wave in the graded HEC chain, as shown in Fig. 5.10. The red curves represent cutoff frequencies of the band structures, also denoted in Fig. 5.10(c) and (d) for the thinning and thickening chains, respectively. From Fig. 5.10(a) and (b), we observe that the power spectral density tends to follow the first and second passing bands of the dispersion curves (compare Fig. 5.10(a) and (c) for thinning and Fig. 5.10(b) and (d) for thickening HEC chain). This means that the propagating wave is mostly composed of the first and second vibrational modes of the HEC. The higher modes are not as evident as the lower ones, especially in the thickening chain, partly due to material damping of PLA.

Figure 5.10(e) and (f) show the spatial spectrum in the thinning and the thickening chain, respectively. The spatial spectrum in the thinning HEC chain gradually includes high wavenumbers as time passes, which is consistent with the stiffening wave front as shown in Fig. 5.2(e). The widely expanded wave front with barely moving wave peak in the thickening HEC chain in Fig. 5.2(f) is well represented in Fig. 5.10(f). The wavenumber is more localized to low region as the wave width expands while the wide spectrum still exists even when the wave reaches the end for the localized peak.

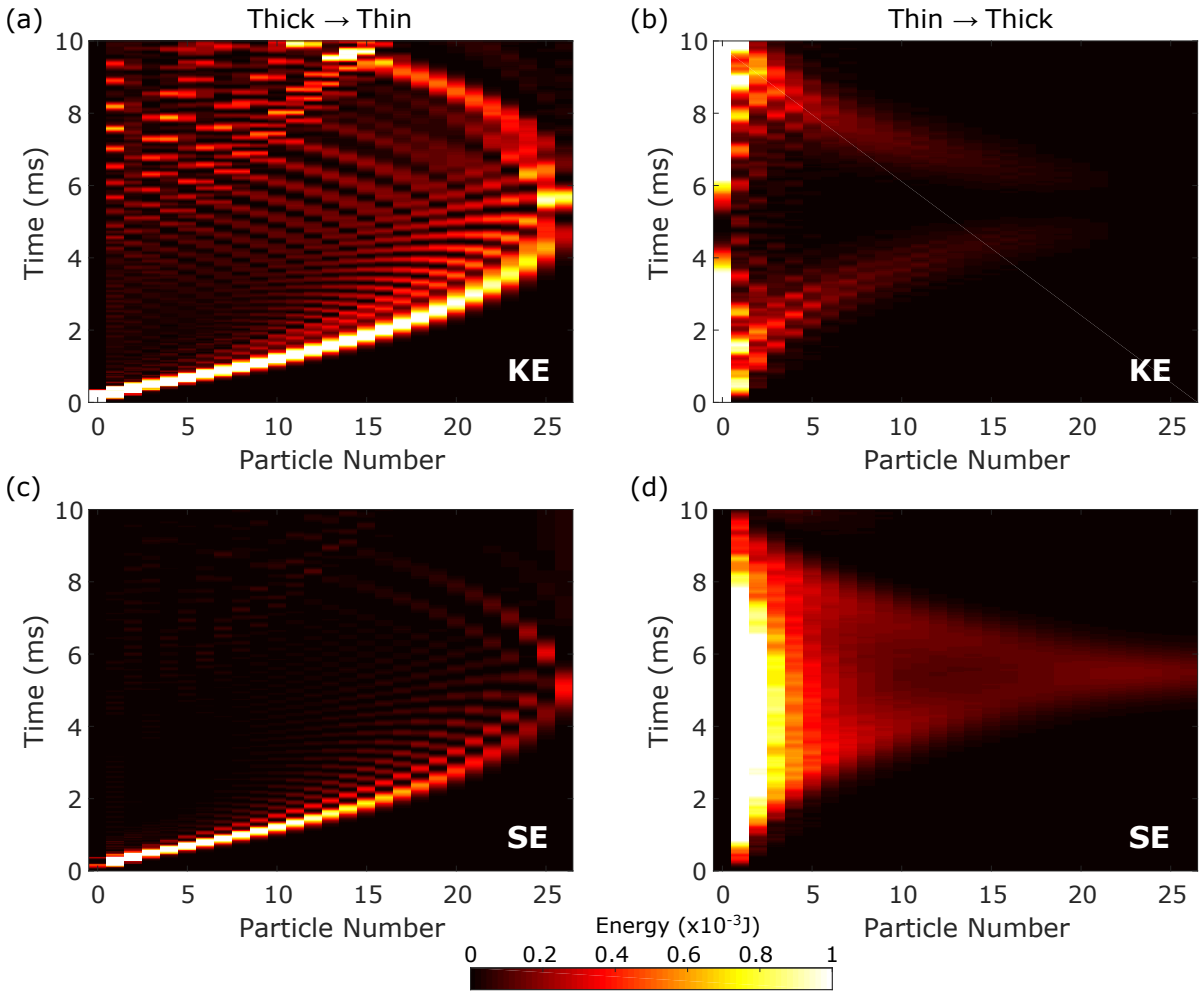

Figure 5.9: The evolution of kinetic energy (KE) and strain energy (SE) is plotted for thinning chain in (a) and (c) and for thickening chain in (b) and (d), respectively. The energy is calculated in ABAQUS simulations without damping. 0 index means the striker.

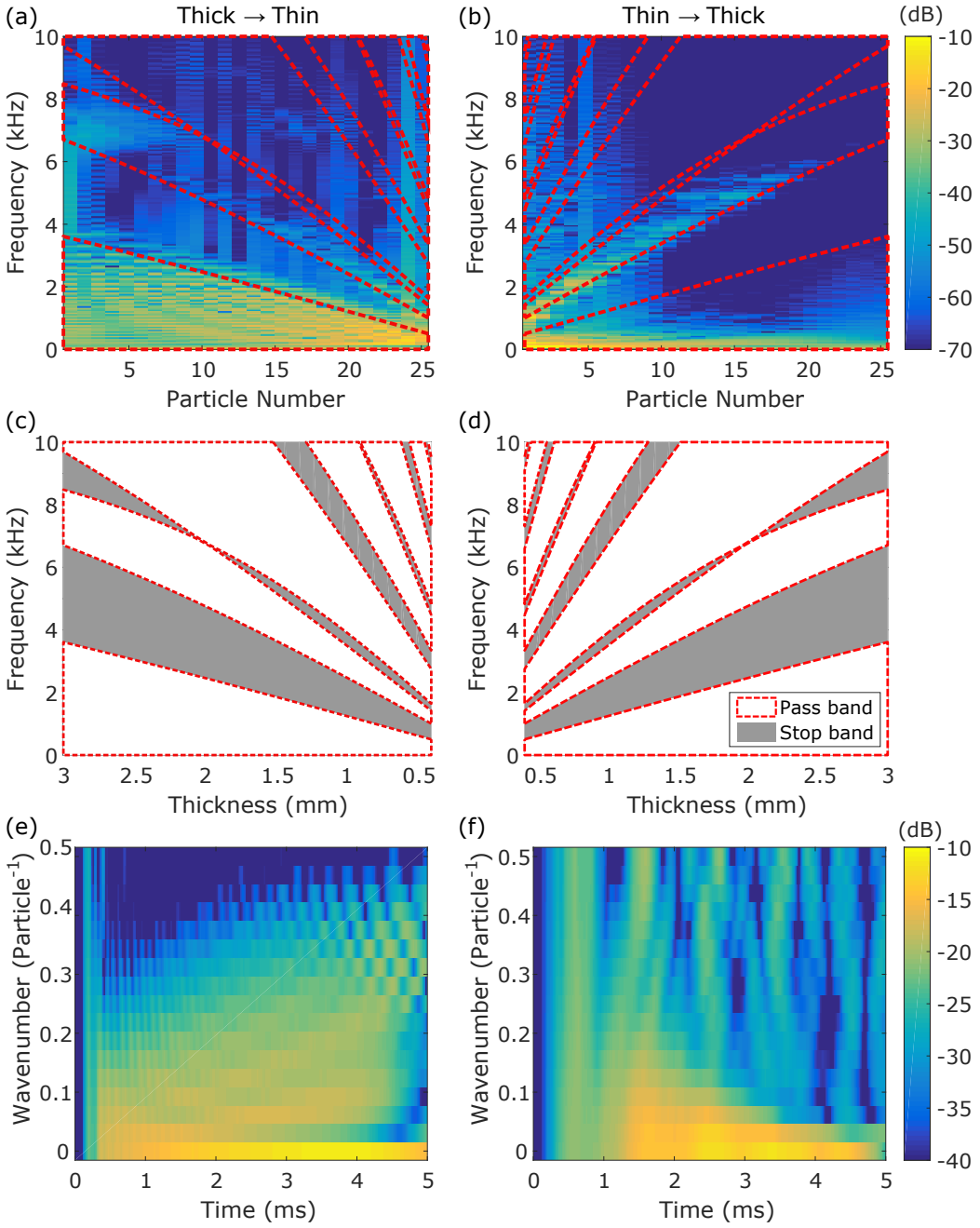

Figure 5.10: Spectral contour of the velocity data from FEA without damping is calculated using Fast Fourier Transform (FFT) in time domain for (a) the thinning and (b) the thickening chain. The red dashed boxes represent the pass bands obtained from the band structures in (c) and (d) for an infinite thinning and thickening chain, respectively. Spatial spectrum of the velocity data is also calculated using FFT in space domain for (e) the thinning and (f) the thickening chain up to 5 ms around when the wave peak reaches the end of the chain.

5.6 Conclusion

We investigated nonlinear dynamic behavior of the graded lattice made of hollow elliptical cylinders (HECs). We experimentally and numerically demonstrated the asymmetric wave dynamics under the condition of external impact applied in opposite directions. This includes acceleration/deceleration and attenuation/amplification of the mechanical wave in terms of velocities, depending on whether the system has a positive or negative gradient of mass and stiffness imposed on the HEC chain. We also investigated the force transmission through the one-dimensional chain, whose trend is seemingly flipped with respect to the velocity profiles. We explained this contradictory behavior by energy analysis. We extended our findings from the 1D system to the 2D array, and demonstrated the efficacy of this asymmetric wave dynamics for impact mitigation purposes. This expansion in 2D space sheds light on a new way to design sandwich core structures for controllable stress wave management. Assigning stiffness gradients in both directions of the 2D array is an on-going study and will potentially lead to the manipulation of wave directionality.

Chapter 6

NONLINEAR WAVE PROPAGATION IN 2D HEC

While we have focused on one dimensional chain of hollow elliptical cylinder (HEC) structures in the previous chapters, the HEC system has great potential for constructing two-dimensional (2D) structures with rich wave dynamics by stacking the unit cells in plane. We show preliminary study of the effect of the unit cell geometry and impact condition on the dynamic response of the 2D HEC array.

First, we investigate the geometric effect. We consider three different aspect ratios of the unit cells, 3:5, 4:4, and 5:3. Here, we define the aspect ratio of the ellipse as $a : b$ where a is the horizontal length and b is the vertical length. The horizontal direction is coaxial to the impact direction. We apply an impact with a striker in all three cases and inspect a snap shot, as shown in Fig. 6.1(a)-(c). We can clearly notice that the wave direction drastically changes depending on the aspect ratio of the HEC unit cell. To calculate the propagation angle, we map the displacement (Fig. 6.1(d)-(f)). We find peak location in each column and apply linear fitting up to the range where the deviation from the fitted line to the peak location is marginal. The angle between the transverse axis and the fitted line is defined as the propagation angle. We observe that the bigger the aspect ratio, the higher the propagation angle.

Next, we explore how the impact condition affects the response of the 2D HEC array. We consider three different combinations of striker mass and input velocity, (a) $m_s = 10m$ and $v_s = 60$ m/s, (b) $m_s = 50m$ and $v_s = 60$ m/s, (c) $m_s = 50m$ and $v_s = 10$ m/s (Fig. 6.2(a)-(c)) where $m = 0.456$ g. We keep the aspect ratio the same as $a : b = 5 : 3$. We repeat the same analysis procedure as the aspect ratio study to find the wave direction. We can clearly see that the striker impact condition also determines the directionality of the wave. When the

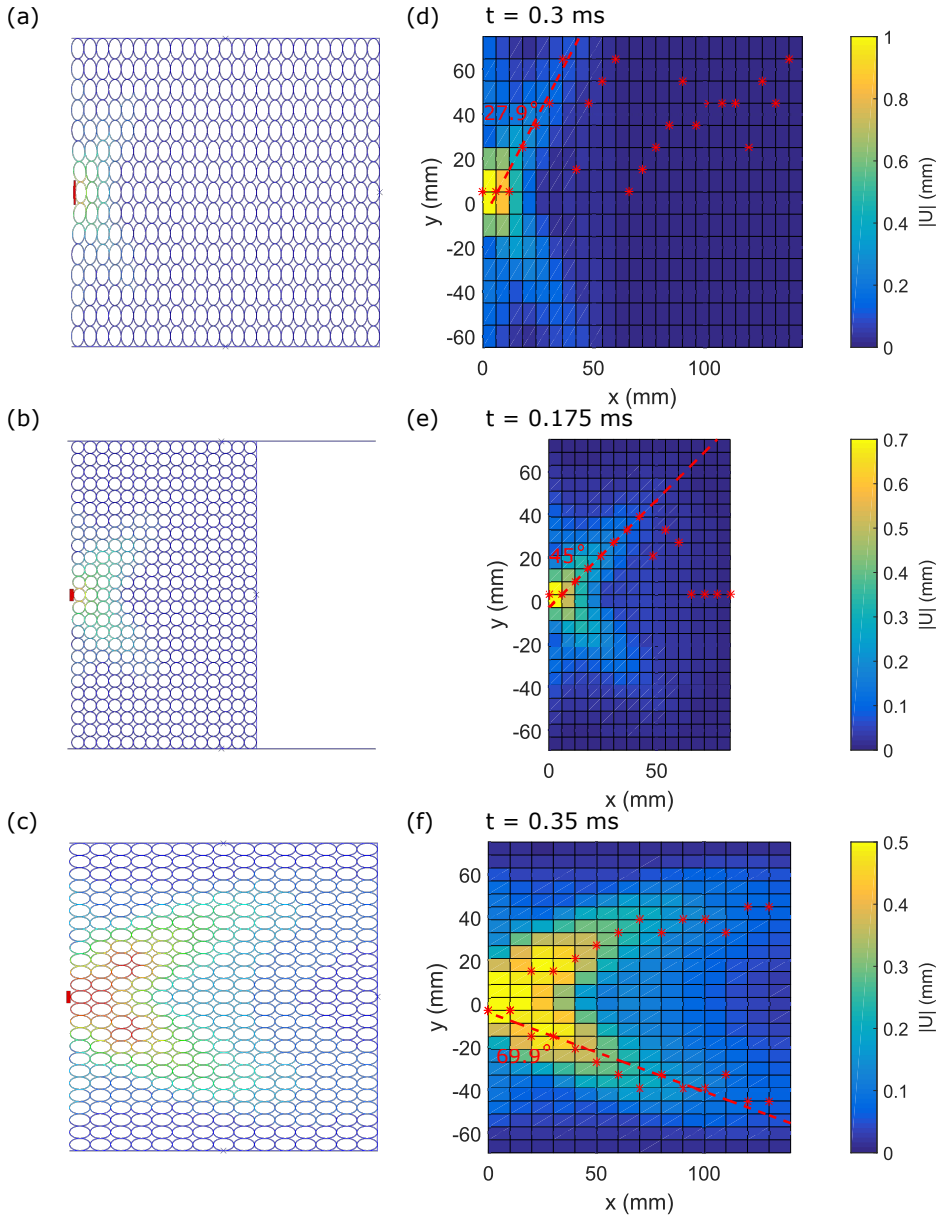

Figure 6.1: A snap shot of the impact analysis on 2D HEC array from the FEM simulation for $m_s = 50m$ and $v_s = 10$ m/s where m_s is striker mass, m is the unit HEC mass, and v_s is striker velocity. The color represent displacement. The array is composed of HEC with aspect ratio (a) 3/5, (b) 4/4, and (c) 5/3. The unit cell mass is identical in all three cases. Displacement contour at the corresponding configuration is shown on their right in (d),(e), and (f). The red asterisks are local peaks at each column. The red dash lines indicate the direction of wave propagation. We choose the time frame to measure the direction when the wave reaches either boundary.

striker mass is bigger (compare Fig. 6.2(e) to (d)) or the input velocity is higher (compare Fig. 6.2(e) to (f)), the wave keeps its direction farther probably due to higher momentum. As a result, the wave reaches the boundary much later than when the momentum is smaller. We also observe that the higher the momentum, the smaller the propagation angle.

At last, we perform parametric study for both the aspect ratio and the input condition and plot all together in Fig. 6.3. The propagating angle tends to be governed by the aspect ratio of the HEC unit cell, although the impact condition also makes small deviations in the directions as well.

In conclusion, we analyze the dynamic response of the 2D HEC lattice under striker impacts. The aspect ratio of the unit hollow ellipse significantly affects the direction of the wave propagation. Basically, the wave direction tends to follow the vertex of the unit hollow ellipse. In addition, under higher striker impact, i.e., higher momentum of the striker, the wave tends to sustain its directionality. The change in the impact condition results in small variation in the direction of the impact wave.

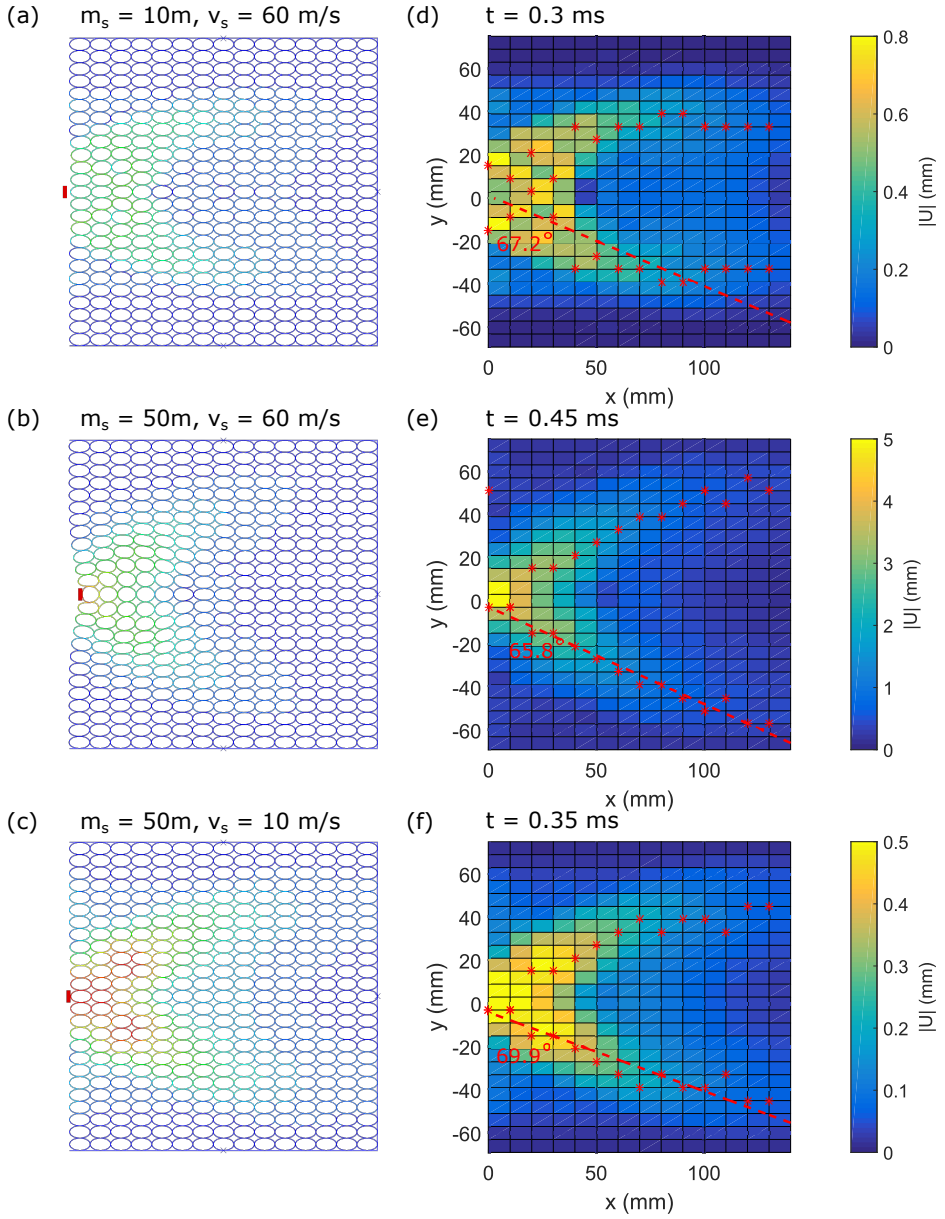

Figure 6.2: A snap shot of the impact analysis on 2D HEC array from the FEM simulation for (a) $m_s = 10m$ and $v_s = 60$ m/s, (b) $m_s = 50m$ and $v_s = 60$ m/s, (c) $m_s = 50m$ and $v_s = 10$ m/s. The aspect ration is $a : b = 5 : 3$. The color represent displacement. Displacement contour at the corresponding condition is shown on their right in (d), (e), and (f). ((c) and (f) are repeated from Fig. 6.1(c) and (f) for easy comparison. The red asterisks are local peaks at each column. The red dash lines indicate the direction of wave propagation.)

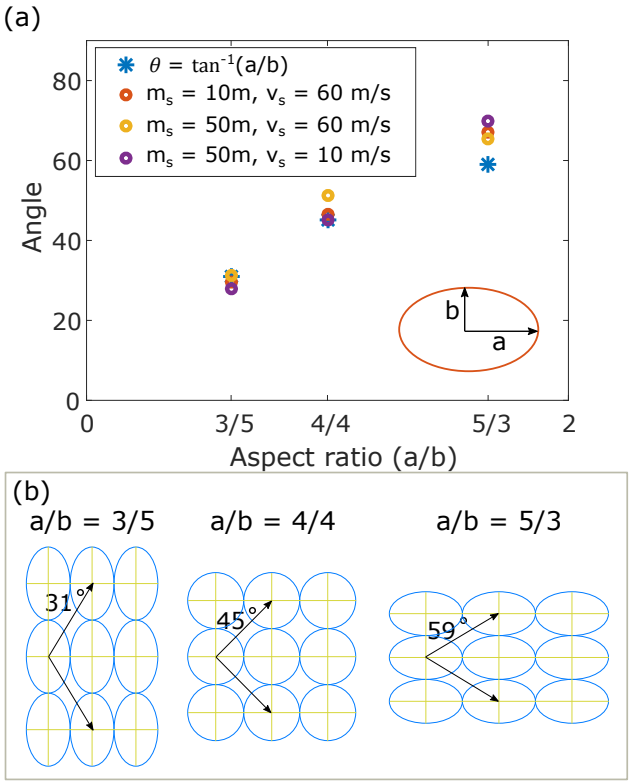

Figure 6.3: (a) The wave propagation angle in 2D HEC array in various configurations at different striker input conditions. (b) The schematic of the configurations considered in (a). The angles represent the diagonal angle with respect to the transverse direction.

Chapter 7
CONCLUSION AND OUTLOOK OF HEC

We have numerically and experimentally explored unique statics and dynamics of 3D-printed HEC structures. In the homogeneous HEC chains, we have found the following features:

- The hollow elliptical cylinders (HECs) show strain-softening behavior in the force-displacement relationship, where the contact stiffness decreases with deformation. This unique nonlinearity comes from the geometry of the HECs (Chapter 2).

- The HEC chain generates dispersive rarefaction shock waves under striker impact, which we verify in experiment. The unique characteristics of the dispersive rarefaction shocks, (a) backward-tilted shape of the leading pulse (rarefaction segment) and (b) the breakage of the wave tails in to a modulated waveform (shock segment), serve as a highly efficient impact mitigation system (Chapter 3).

- The HECs can be approximated into a one degree-of-freedom spring-mass system (Chapter 2 and Chapter 3). We numerically verify that the discrete element method using this approximation can fairly predict nonlinear wave dynamics in the HEC chain (Chapter 3).

By leveraging the tunability given from 3D-printing, we impose gradient in the mass/stiffness of HECs and further explore elastic wave dynamics. The important findings from the graded HEC structures are summarized as follows:

- The negatively graded HEC chain traps elastic waves at a specific location, which depends on the input frequency of the propagating waves. This is based on the principle

of the Bloch oscillations discovered originally in the quantum mechanics of electrons (Chapter 4).

- The positively graded HEC chain reflects elastic waves back at different locations at different input frequency of the waves (Chapter 4).

- The graded HEC chain shows asymmetric wave dynamics under striker impact. The positively graded HEC chain accelerates the propagating wave, while the opposite happens in the negatively graded HEC chain (Chapter 5).

- Compared to the positively graded HEC chain, the negatively graded HEC chain shows near an order-of-magnitude difference in terms of transmitted force amplitudes (Chapter 5).

We have shown that we can easily assemble the HECs into a 2D lattice. Below is a couple of facts we have found:

- We suggest the 2D graded HEC lattice as a core material in sandwich structures, based on its significant energy attenuation we observe (Chapter 5).

- Shock wave propagation in 2D HEC lattice is governed by the aspect ratio of the unit HECs. The higher impact tends to keep its direction farther in the array (Chapter 6).

In this study, HEC structure has been fabricated only by PLA. To develop practical engineering applications, new materials such as metal or soft or rubbery materials can be explored. The 3D-printer used in this study is an off-the-shelf printer and supports not only PLA but also Nylon, ABS (acrylonitrile butadiene styrene), PVA (polyvinyl alcohol), TPU (thermoplastic polyurethane) 95A, PP (polypropylene), PC (polycarbonate), and CPE (copolyester). As the 3D-printing evolves, much more variety in material section is expected.

Wave directionality in 2D HEC lattice can be an interesting topic to explore. Although we only discuss dispersion relations in one direction in this work, we will see more complex

dispersion surfaces in 2D space. By leveraging partial band gaps, we can effectively control the direction of wave propagation.

We can give a variation in the chain composition. Dimer chain using alternating unit cells with two different geometry could create interesting wave dynamics. As we have done in this work, we can impose difference in the the aspect ratio or the thickness of the HECs.

BIBLIOGRAPHY

[1] H. Kim, E. Kim, C. Chong, P. G. Kevrekidis, and J. Yang. Demonstration of dispersive rarefaction shocks in hollow elliptical cylinder chains. *Phys. Rev. Lett.*, 120:194101, May 2018.

[2] Hyunryung Kim, Eunho Kim, and Jinkyu Yang. Nonlinear Wave Propagation in 3D-Printed Graded Lattices of Hollow Elliptical Cylinders. *ArXiv e-prints*, page arXiv:1812.00095, November 2018.

[3] Hyunryung Kim, Xiaotian Shi, Eunho Kim, and Jinkyu Yang. Bloch oscillation of elastic waves in the graded lattice of 3D-printed hollow elliptical cylinders. *arXiv e-prints*, page arXiv:1812.02242, December 2018.

[4] J. S. Uehara, M. A. Ambroso, R. P. Ojha, and D. J. Durian. Low-speed impact craters in loose granular media. *Phys. Rev. Lett.*, 90:194301, May 2003.

[5] R. Martínez-Sala, J. Sancho, J. V. Sánchez, V. Gómez, J. Llinares, and F. Meseguer. Sound attenuation by sculpture. *Nature*, 378:241, Nov 1995.

[6] Manvir S. Kushwaha. Stop-bands for periodic metallic rods: Sculptures that can filter the noise. *Applied Physics Letters*, 70(24):3218–3220, 1997.

[7] M. Carrara, M. R. Cacan, M. J. Leamy, M. Ruzzene, and A. Erturk. Dramatic enhancement of structure-borne wave energy harvesting using an elliptical acoustic mirror. *Applied Physics Letters*, 100(20):204105, 2012.

[8] V. F. Nesterenko. *Dynamics Of heterogeneous materials*. Springer-Verlag New York Inc., 2001.

[9] S. Sen, J. Hong, J. Bang, E. Avalos, and R. Doney. Solitary waves in the granular chain. *Physics Reports*, 462(2):21–66, 2008.

[10] S. Flach and C.R. Willis. Discrete breathers. *Physics Reports*, 295(5):181 – 264, 1998.

[11] C Chong, Mason A Porter, P G Kevrekidis, and C Daraio. Nonlinear coherent structures in granular crystals. *Journal of Physics: Condensed Matter*, 29(41):413003, 2017.

[12] G. Theocharis, N. Boechler, and C. Daraio. *Nonlinear Periodic Phononic Structures and Granular Crystals*, pages 217–251. Springer Berlin Heidelberg, Berlin, Heidelberg, 2013.

[13] Yuli Starosvetsky, K R Jayaprakash, M Arif Hasan, and Alexander F Vakakis. *Topics on the Nonlinear Dynamics and Acoustics of Ordered Granular Media*. WORLD SCIENTIFIC, 2017.

[14] E. B. Herbold and V. F. Nesterenko. Shock wave structure in a strongly nonlinear lattice with viscous dissipation. *Phys. Rev. E*, 75:021304, Feb 2007.

[15] Alain Molinari and Chiara Daraio. Stationary shocks in periodic highly nonlinear granular chains. *Phys. Rev. E*, 80:056602, Nov 2009.

[16] Leopoldo R. Gómez, Ari M. Turner, and Vincenzo Vitelli. Uniform shock waves in disordered granular matter. *Phys. Rev. E*, 86:041302, Oct 2012.

[17] B. Edward McDonald and David Calvo. Simple waves in hertzian chains. *Phys. Rev. E*, 85:066602, Jun 2012.

[18] K. L. Johnson. *Contact Mechanics*. Cambridge University Press, 1985.

[19] E. B. Herbold and V. F. Nesterenko. Propagation of rarefaction pulses in discrete materials with strain-softening behavior. *Phys. Rev. Lett.*, 110:144101, Apr 2013.

[20] H. Yasuda, C. Chong, J. Yang, and P. G. Kevrekidis. Emergence of dispersive shocks and rarefaction waves in power-law contact models. *Phys. Rev. E*, 95:062216, Jun 2017.

[21] Fernando Fraternali, Gerardo Carpentieri, Ada Amendola, Robert E. Skelton, and Vitali F. Nesterenko. Multiscale tunability of solitary wave dynamics in tensegrity metamaterials. *Applied Physics Letters*, 105(20):201903, 2014.

[22] H. Yasuda, C. Chong, E. G. Charalampidis, P. G. Kevrekidis, and J. Yang. Formation of rarefaction waves in origami-based metamaterials. *Phys. Rev. E*, 93:043004, Apr 2016.

[23] Felix Bloch. Über die quantenmechanik der elektronen in kristallgittern. *Zeitschrift für Physik*, 52(7):555–600, Jul 1929.

[24] A theory of the electrical breakdown of solid dielectrics. *Proceedings of the Royal Society of London A: Mathematical, Physical and Engineering Sciences*, 145(855):523–529, 1934.

[25] Walter Kohn. Theory of bloch electrons in a magnetic field: The effective hamiltonian. *Phys. Rev.*, 115:1460–1478, Sep 1959.

[26] Gregory H. Wannier. Wave functions and effective hamiltonian for bloch electrons in an electric field. *Phys. Rev.*, 117:432–439, Jan 1960.

[27] L. Esaki and R. Tsu. Superlattice and negative differential conductivity in semiconductors. *IBM Journal of Research and Development*, 14(1):61–65, Jan 1970.

[28] E. E. Mendez, F. Agulló-Rueda, and J. M. Hong. Stark localization in gaas-gaalas superlattices under an electric field. *Phys. Rev. Lett.*, 60:2426–2429, Jun 1988.

[29] J. Bleuse, G. Bastard, and P. Voisin. Electric-field-induced localization and oscillatory electro-optical properties of semiconductor superlattices. *Phys. Rev. Lett.*, 60:220–223, Jan 1988.

[30] L. S. Kuzmin and D. B. Haviland. Observation of the bloch oscillations in an ultrasmall josephson junction. *Phys. Rev. Lett.*, 67:2890–2893, Nov 1991.

[31] J. Feldmann, K. Leo, J. Shah, D. A. B. Miller, J. E. Cunningham, T. Meier, G. von Plessen, A. Schulze, P. Thomas, and S. Schmitt-Rink. Optical investigation of bloch oscillations in a semiconductor superlattice. *Phys. Rev. B*, 46:7252–7255, Sep 1992.

[32] Karl Leo, Peter Haring Bolivar, Frank Brggemann, Ralf Schwedler, and Klaus Khler. Observation of bloch oscillations in a semiconductor superlattice. *Solid State Communications*, 84(10):943 – 946, 1992.

[33] Christian Waschke, Hartmut G. Roskos, Ralf Schwedler, Karl Leo, Heinrich Kurz, and Klaus Köhler. Coherent submillimeter-wave emission from bloch oscillations in a semiconductor superlattice. *Phys. Rev. Lett.*, 70:3319–3322, May 1993.

[34] T. Dekorsy, P. Leisching, K. Köhler, and H. Kurz. Electro-optic detection of bloch oscillations. *Phys. Rev. B*, 50:8106–8109, Sep 1994.

[35] R. Martini, G. Klose, H. G. Roskos, H. Kurz, H. T. Grahn, and R. Hey. Superradiant emission from bloch oscillations in semiconductor superlattices. *Phys. Rev. B*, 54:R14325–R14328, Nov 1996.

[36] F. Löser, Yu. A. Kosevich, K. Köhler, and K. Leo. Dynamics of bloch oscillations under the influence of scattering and coherent plasmon coupling. *Phys. Rev. B*, 61:R13373–R13376, May 2000.

[37] T. Pertsch, P. Dannberg, W. Elflein, A. Bräuer, and F. Lederer. Optical bloch oscillations in temperature tuned waveguide arrays. *Phys. Rev. Lett.*, 83:4752–4755, Dec 1999.

[38] R. Morandotti, U. Peschel, J. S. Aitchison, H. S. Eisenberg, and Y. Silberberg. Experimental observation of linear and nonlinear optical bloch oscillations. *Phys. Rev. Lett.*, 83:4756–4759, Dec 1999.

[39] Riccardo Sapienza, Paola Costantino, Diederik Wiersma, Mher Ghulinyan, Claudio J. Oton, and Lorenzo Pavesi. Optical analogue of electronic bloch oscillations. *Phys. Rev. Lett.*, 91:263902, Dec 2003.

[40] V. Agarwal, J. A. del Río, G. Malpuech, M. Zamfirescu, A. Kavokin, D. Coquillat, D. Scalbert, M. Vladimirova, and B. Gil. Photon bloch oscillations in porous silicon optical superlattices. *Phys. Rev. Lett.*, 92:097401, Mar 2004.

[41] Virginie Lousse and Shanhui Fan. Tunable terahertz bloch oscillations in chirped photonic crystals. *Phys. Rev. B*, 72:075119, Aug 2005.

[42] Mher Ghulinyan, Claudio J. Oton, Zeno Gaburro, Lorenzo Pavesi, Costanza Toninelli, and Diederik S. Wiersma. Zener tunneling of light waves in an optical superlattice. *Phys. Rev. Lett.*, 94:127401, Mar 2005.

[43] Arash Joushaghani, Rajiv Iyer, Joyce K. S. Poon, J. Stewart Aitchison, C. Martijn de Sterke, Jun Wan, and Marc M. Dignam. Quasi-bloch oscillations in curved coupled optical waveguides. *Phys. Rev. Lett.*, 103:143903, Oct 2009.

[44] N. D. Lanzillotti Kimura, A. Fainstein, and B. Jusserand. Phonon bloch oscillations in acoustic-cavity structures. *Phys. Rev. B*, 71:041305, Jan 2005.

[45] Helios Sanchis-Alepuz, Yuriy A. Kosevich, and José Sánchez-Dehesa. Acoustic analogue of electronic bloch oscillations and resonant zener tunneling in ultrasonic superlattices. *Phys. Rev. Lett.*, 98:134301, Mar 2007.

[46] N. D. Lanzillotti-Kimura, A. Fainstein, B. Perrin, B. Jusserand, O. Mauguin, L. Largeau, and A. Lemaître. Bloch oscillations of thz acoustic phonons in coupled nanocavity structures. *Phys. Rev. Lett.*, 104:197402, May 2010.

[47] Zhaojian He, Shasha Peng, Feiyan Cai, Manzhu Ke, and Zhengyou Liu. Acoustic bloch oscillations in a two-dimensional phononic crystal. *Phys. Rev. E*, 76:056605, Nov 2007.

[48] M. M. de Lima, Yu. A. Kosevich, P. V. Santos, and A. Cantarero. Surface acoustic bloch oscillations, the wannier-stark ladder, and landau-zener tunneling in a solid. *Phys. Rev. Lett.*, 104:165502, Apr 2010.

[49] A. A. Karabutov, Yu. A. Kosevich, and O. A. Sapozhnikov. Bloch oscillations of an acoustic field in a layered structure. *Acoustical Physics*, 59(2):137–147, Mar 2013.

[50] Z. Lazcano and J. Arriaga. Acoustic wannier-stark ladders and bloch oscillations in porous silicon structures. *Applied Physics Letters*, 105(23):231901, 2014.

[51] L. Gutiérrez, A. Díaz-de Anda, J. Flores, R. A. Méndez-Sánchez, G. Monsivais, and A. Morales. Wannier-stark ladders in one-dimensional elastic systems. *Phys. Rev. Lett.*, 97:114301, Sep 2006.

[52] A. Arreola-Lucas, G. Báez, F. Cervera, A. Climente, R. A. Méndez-Sánchez, and J. Sánchez-Dehesa. Mechanical Rainbow Trapping and Bloch Oscillations in Structured Elastic Beams. *ArXiv e-prints*, July 2017.

[53] Xiaotian Shi, Rajesh Chaunsali, Ying Wu, and Jinkyu Yang. Elastic wannier-stark ladders and bloch oscillations in 1d granular crystals. *Journal of Applied Physics*, 123(10):104904, 2018.

[54] Alexandre Rosas and Katja Lindenberg. Pulse propagation in granular chains. *Physics Reports*, 735:1 – 37, 2018.

[55] Surajit Sen, Felicia S. Manciu, and Marian Manciu. Thermalizing an impulse. *Physica A: Statistical Mechanics and its Applications*, 299(3):551 – 558, 2001.

[56] David T Wu. Conservation principles in solitary impulse propagation through granular chains. *Physica A: Statistical Mechanics and its Applications*, 315(1):194 – 202, 2002. Slow Dynamical Processes in Nature.

[57] Robert L. Doney and Surajit Sen. Impulse absorption by tapered horizontal alignments of elastic spheres. *Phys. Rev. E*, 72:041304, Oct 2005.

[58] Upendra Harbola, Alexandre Rosas, Massimiliano Esposito, and Katja Lindenberg. Pulse propagation in tapered granular chains: An analytic study. *Phys. Rev. E*, 80:031303, Sep 2009.

[59] L. P. Machado, Alexandre Rosas, and Katja Lindenberg. Momentum and energy propagation in tapered granular chains. *Granular Matter*, 15(6):735–746, Dec 2013.

[60] Adam Sokolow, Jan M. M. Pfannes, Robert L. Doney, Masami Nakagawa, Juan H. Agui, and Surajit Sen. Absorption of short duration pulses by small, scalable, tapered granular chains. *Applied Physics Letters*, 87(25):254104, 2005.

[61] Masami Nakagawa, Juan H. Agui, David T. Wu, and David Vivanco Extramiana. Impulse dispersion in a tapered granular chain. *Granular Matter*, 4(4):167–174, Feb 2003.

[62] Francisco Melo, Stéphane Job, Francisco Santibanez, and Franco Tapia. Experimental evidence of shock mitigation in a hertzian tapered chain. *Phys. Rev. E*, 73:041305, Apr 2006.

[63] Robert Doney and Surajit Sen. Decorated, tapered, and highly nonlinear granular chain. *Phys. Rev. Lett.*, 97:155502, Oct 2006.

[64] Robert L. Doney, Juan H. Agui, and Surajit Sen. Energy partitioning and impulse dispersion in the decorated, tapered, strongly nonlinear granular alignment: A system with many potential applications. *Journal of Applied Physics*, 106(6):064905, 2009.

[65] Upendra Harbola, Alexandre Rosas, Aldo H. Romero, Massimiliano Esposito, and Katja Lindenberg. Pulse propagation in decorated granular chains: An analytical approach. *Phys. Rev. E*, 80:051302, Nov 2009.

[66] L. P. Machado, A. Rosas, and K. Lindenberg. A quasi-unidimensional granular chain to attenuate impact. *The European Physical Journal E*, 37(11):119, Nov 2014.

[67] Mukesh Tiwari, T. R. Krishna Mohan, and Surajit Sen. Decorated granular layers for impact decimation. *Granular Matter*, 18(3):45, May 2016.

[68] Surajit Sen, T. R. Krishna Mohan, and Mukesh Tiwari. Impact dispersion using 2d and 3d composite granular packing. *KONA Powder and Particle Journal*, 34:248–257, 2017.

[69] A. Tsouknidas, M. Pantazopoulos, I. Katsoulis, D. Fasnakis, S. Maropoulos, and N. Michailidis. Impact absorption capacity of 3d-printed components fabricated by fused deposition modelling. *Materials and Design*, 102:41 – 44, 2016.

[70] Simon R.G. Bates, Ian R. Farrow, and Richard S. Trask. 3d printed polyurethane honeycombs for repeated tailored energy absorption. *Materials and Design*, 112:172 – 183, 2016.

[71] Liming Chen, Jian Zhang, Bing Du, Hao Zhou, Houchang Liu, Yongguang Guo, Weiguo Li, and Daining Fang. Dynamic crushing behavior and energy absorption of graded lattice cylindrical structure under axial impact load. *Thin-Walled Structures*, 127:333 – 343, 2018.

[72] Nicholas W. Bartlett, Michael T. Tolley, Johannes T. B. Overvelde, James C. Weaver, Bobak Mosadegh, Katia Bertoldi, George M. Whitesides, and Robert J. Wood. A 3d-printed, functionally graded soft robot powered by combustion. *Science*, 349(6244):161–165, 2015.

[73] B. Deng, J. R. Raney, V. Tournat, and K. Bertoldi. Elastic vector solitons in soft architected materials. *Phys. Rev. Lett.*, 118:204102, May 2017.

[74] Sicong Shan, Sung H. Kang, Jordan R. Raney, Pai Wang, Lichen Fang, Francisco Candido, Jennifer A. Lewis, and Katia Bertoldi. Multistable architected materials for trapping elastic strain energy. *Advanced Materials*, 27(29):4296–4301.

[75] Dingzeyu Li, David I. W. Levin, Wojciech Matusik, and Changxi Zheng. Acoustic voxels: Computational optimization of modular acoustic filters. *ACM Trans. Graph.*, 35(4):88:1–88:12, July 2016.

[76] Neel Nadkarni, Andres F. Arrieta, Christopher Chong, Dennis M. Kochmann, and Chiara Daraio. Unidirectional transition waves in bistable lattices. *Phys. Rev. Lett.*, 116:244501, Jun 2016.

[77] Hongbin Fang, K.W. Wang, and Suyi Li. Asymmetric energy barrier and mechanical diode effect from folding multi-stable stacked-origami. *Extreme Mechanics Letters*, 17:7 – 15, 2017.

[78] Z. Wu, Y. Zheng, and K. W. Wang. Metastable modular metastructures for on-demand reconfiguration of band structures and nonreciprocal wave propagation. *Phys. Rev. E*, 97:022209, Feb 2018.

[79] Z. Wu and K.-W. Wang. On the wave propagation analysis and supratransmission prediction of a metastable modular metastructure for adaptive non-reciprocal energy transmission. *ArXiv e-prints*, September 2017.

[80] A.F. Bower. *Applied Mechanics of Solids*. CRC Press, 2009.

[81] W. Chen, F. Lu, and M. Cheng. Tension and compression tests of two polymers under quasi-static and dynamic loading. *Polymer Testing*, 21(2):113 – 121, 2002.

[82] Nishida, M., Yamaguchi, M., Todo, M., Takayama, T., Häggblad, H.-Å., and Jonsén, P. Evaluation of dynamic compressive properties of pla polymer blends using split hopkinson pressure bar. *DYMAT - International Conference on the Mechanical and Physical Behaviour of Materials under Dynamic Loading*, 1:909–915, 2009.

[83] L. Brillouin. *Wave propagation in periodic structures: electric filters and crystal lattices*. Dover books and science. Dover Publications, 1953.

[84] G. El, M. Hoefer, and M. Shearer. Dispersive and diffusive-dispersive shock waves for nonconvex conservation laws. *SIAM Review*, 59(1):3–61, 2017.

[85] G. Biondini, G.A. El, M.A. Hoefer, and P.D. Miller. Dispersive hydrodynamics: Preface. *Physica D: Nonlinear Phenomena*, 333:1 – 5, 2016. Dispersive Hydrodynamics.

[86] Melanie Senn. This open source code is used for dic tracking https://www.mathworks.com/matlabcentral/fileexchange/50994-digital-image-correlation-and-tracking, 2015.

[87] E. Kim, F. Li, C. Chong, G. Theocharis, J. Yang, and P. G. Kevrekidis. Highly nonlinear wave propagation in elastic woodpile periodic structures. *Phys. Rev. Lett.*, 114:118002, Mar 2015.

[88] Mason Porter, Panayotis Kevrekidis, and Chiara Darario. Granular crystals: Nonlinear dynamics meets materials engineering. *Physics Today*, 68:44, 2015.

[89] Kosmas L. Tsakmakidis, Allan D. Boardman, and Ortwin Hess. 'trapped rainbow' storage of light in metamaterials. *Nature*, 450:397–401, Nov 2007.

[90] R. Chaunsali, E. Kim, and J. Yang. Demonstration of accelerating and decelerating nonlinear impulse waves in functionally graded granular chains. *Philosophical Transactions of the Royal Society of London A: Mathematical, Physical and Engineering Sciences*, 2018.

VITA

Hyunryung (Helen) Kim was born in Iksan, Jeollabuk-do, South Korea. She earned her B.S. in Mechanical Engineering in 2012 and M.S. in Mechanical Engineering in 2014 from Yonsei University, Seoul, South Korea. In Autumn 2014, she joined the Laboratory for Engineered Materials and Structures (LEMS), led by Professor Jinkyu Yang, at the University of Washington, Seattle, WA, USA. She was awarded the UW college of Engineering Dean's Fellowship in 2014 and Amelia Earhart Fellowship in 2017. In 2018, she earned a Ph.D. degree in Aeronautics & Astronautics from the University of Washington, Seattle, WA, USA.